AMBIGUITY RESOLUTION ALGORITHMS FOR DIRECTION OF ARRIVAL ESTIMATION

A THESIS SUBMITTED TO
THE GRADUATE SCHOOL OF NATURAL AND APPLIED SCIENCES
OF
MIDDLE EAST TECHNICAL UNIVERSITY

BY

İLKER EROL

IN PARTIAL FULFILLMENT OF THE REQUIREMENTS
FOR
THE DEGREE OF MASTER OF SCIENCE
IN
ELECTRICAL AND ELECTRONIC ENGINEERING

NOVEMBER 2024

Approval of the thesis:

AMBIGUITY RESOLUTION ALGORITHMS FOR DIRECTION OF ARRIVAL ESTIMATION

submitted by **İLKER EROL** in partial fulfillment of the requirements for the degree of **Master of Science** i**n Electrical and Electronic Engineering, Middle East Technical University** by,

Prof. Dr. Naci Emre Altun
Dean, **Graduate School of Natural and Applied Sciences** _____

Prof. Dr. İlkay Ulusoy
Head of the Department, **Electrical and Electronics Eng.** _____

Prof. Dr. T.Engin Tuncer
Supervisor, **Electrical and Electronics Engineering, METU** _____

Examining Committee Members:

Prof. Dr. Ali Özgür Yılmaz
Electrical and Electronics Eng., METU _____

Prof. Dr. T.Engin Tuncer
Electrical and Electronics Eng., METU _____

Assist. Prof. Dr. Özlem Tuğfe Demir
Electrical and Electronics Eng., TOBB ETU _____

Date: 29.11.2024

I hereby declare that all information in this document has been obtained and presented in accordance with academic rules and ethical conduct. I also declare that, as required by these rules and conduct, I have fully cited and referenced all material and results that are not original to this work.

Name Last name : İlker Erol

Signature:

ABSTRACT

AMBIGUITY RESOLUTION ALGORITHMS FOR DIRECTION OF ARRIVAL ESTIMATION

Erol, İlker
Master of Science, Electrical and Electronic Engineering
Supervisor : Prof. Dr. T.Engin Tuncer

November 2024, 92 pages

In direction finding, it is well known that angular accuracy increases as the array aperture increases. However, array aperture cannot be made larger than the theoretical limit which indicates that inter-element spacing should be less than half the wavelength. In the literature, there are methods which overcome this limit with a trade off on the array robustness for different distortions. In this thesis, ambiguity resolution techniques are investigated and a new array structure together with an ambiguity resolution method is proposed. More specifically, it is proposed to use SODA geometry in four elements planar structure and rotate the array to cover 360 degrees with high accuracy and isometric response. In this context, different methods of ambiguity resolution such as amplitude and phase comparison methods, Hybrid Amplitude/Phase, Hybrid Amplitude/MUSIC (MUltiple SIgnal Classification), rotating interferometer, and SODA (Second Order Difference Array) interferometer methods are considered and their performances are compared. Considering the potential of the SODA array structure, SODA structure has been modified to have four elements planar form. While this structure has no ambiguity, it is almost close

to a linear array and hence its performance is handicapped in certain directions. In order to remove this deficiency and have an isometric angular response, it is proposed to rotate the array to have 360 degrees of coverage. The Doppler effect due to rotation is accounted for and the performance of a variety of SODA structures are investigated by using both Cramér-Rao Bound (CRB) and simulations. It is shown that the proposed SODA structure is very effective and the array accuracy is significantly high without imposing ambiguity.

Keywords: Direction Finding, Ambiguity Resolution, Soda Array, Interferometer, Rotating Arrays.

ÖZ

GELİŞ YÖNÜ KESTİRİMİ İÇİN BELİRSİZLİK ÇÖZME ALGORİTMALARI

Erol, İlker
Yüksek Lisans, Elektrik ve Elektronik Mühendisliği
Tez Yöneticisi: Prof. Dr. T.Engin Tuncer

Kasım 2024, 92 sayfa

Yön bulmada, anten açıklığının artması ile birlikte açısal doğruluğun da arttığı bilinmektedir. Ancak, açıklık teorik sınırın üzerinde büyütülemez, bu da eleman aralığının dalga boyunun yarısından küçük olması gerektiği anlamına gelir. Literatürde, bu sınırı aşan ancak çeşitli bozulmalar için dizi performansındaki dayanıklılıktan ödün verme gerektiren yöntemler mevcuttur. Bu tezde, belirsizlik çözümleme teknikleri incelenmiş ve bir belirsizlik çözümleme yöntemi ile birlikte yeni bir dizi yapısı önerilmiştir. Daha spesifik olarak, dört elemanlı düzlemsel bir yapıda SODA (İkinci Derece Fark Dizi) geometrisi kullanılmasının ve dizinin 360 derece yüksek doğruluk ve izometrik yanıt ile döndürülmesinin önerildiği bir yöntem sunulmuştur. Bu bağlamda, genlik ve faz karşılaştırma yöntemleri, Hibrit Genlik/Faz, Hibrit Genlik/MUSIC (Çoklu Sinyal Sınıflandırması), dönen interferometre ile SODA (İkinci Derece Fark Dizi) interferometre yöntemleri gibi çeşitli belirsizlik çözümleme yöntemleri ele alınmış ve performansları karşılaştırılmıştır. SODA dizi yapısının potansiyeli dikkate alınarak, SODA yapısı dört elemanlı düzlemsel bir formla değiştirilmiştir. Bu yapı belirsizlik içermese de

doğrusal bir diziye benzemekte ve bu nedenle belirli yönlerde performansı kısıtlanmaktadır. Bu eksikliği gidermek ve izometrik bir açısal yanıt elde etmek için diziyi 360 derece döndürülmesi önerilmiştir. Döndürmenin Doppler etkisi dikkate alınmış ve çeşitli SODA yapıların performansı hem Cramér-Rao Sınırı (CRB) hem de simülasyonlar kullanılarak incelenmiştir. Önerilen SODA yapısının çok etkili olduğu ve dizinin doğruluğunun büyük ölçüde arttığı, belirsizlik oluşturmadan yüksek doğruluk sağladığı gösterilmiştir.

Anahtar Kelimeler: Yön Bulma, Belirsizlik Çözme, Soda Dizisi, Interferometre, Dönen Diziler.

To my precious mother and father

ACKNOWLEDGMENTS

I would like to express my deepest gratitude to my supervisor Prof. Dr. T.Engin Tuncer for his invaluable guidance, insightful feedback, and continuous encouragement throughout this research. His expertise and support have been instrumental in shaping this work.

I want to express my deepest appreciation to my mom and dad for their unwavering support, patience, and understanding. Your encouragement and belief in me have been a source of great strength throughout this journey.

I would also like to thank my colleagues for his suggestions and comments.

TABLE OF CONTENTS

LIST OF TABLES

TABLES

LIST OF FIGURES

FIGURES

LIST OF ABBREVIATIONS

ABBREVIATIONS

DOA	Direction of Arrival
ES	Electronic Surveillance
ESS	Electronics Support System
SODA	Second Order Difference Array
RMSE	Root Mean Square Error
SNR	Signal to Noise Ratio
SVD	Singular Value Decomposition
FOV	Field of View
SBI	SODA-Based Inference

CHAPTER 1

INTRODUCTION

This work aims to investigate diverse techniques for resolving angular ambiguity caused by spatial aliasing for Direction of Arrival (DOA) estimation. In the array signal processing literature, DOA estimation is the crucial technique used for determining the angular positions of the transmitted source signals. This estimation holds significant importance in various applications such as radar, radio astronomy, wireless communications sonar, commutations, direction finding, seismology, medical diagnosis and treatment acoustic systems [1]. Under the scope of this study the array structures of similar working manner passive systems such as Electronic Surveillance (ES), Electronics Support System (ESS) and Anti-Radiation Seeker is examined. Due the fact that these systems are operating at wide frequency range, could have antenna placement and mounting limitation and need an accurate and high DOA performance, the spatial aliasing problem could be emerged.

1.1 DOA Estimation

Electronic Support System is objected to identify the RF radiated target. The flowchart of the operation mechanism of ESS could be summarized as follows. At first the RF radiated targets are detected and separated with each other's. Then RF characteristics of the selected target are measured and correlated with other probable target RF threat sensor parameters stored in the mission data file which enables the identification of the RF target. The angular position information is also provided and in some cases the location of targets could be monitored with implementing

localization algorithms [2]. The typical ESS operating requirements can be summarized as follows [3]

- Operating in real-time at a wide-band frequency range for center frequency as 2-18 GHz
- Having capability to observe a wide instantaneous bandwidth 500 MHz or more
- To have a high probability of detection and low receiver noise figure
- To be able to identify multi RF target
- Be affordable cost

The RF characteristics such as pulse amplitude, pulse width, time of arrival, RF center frequency and direction of arrival are able to be measured by ESS. The DOA is the signification parameter for ESS because the angular position of RF target signal cannot change in pulse to pulse manner which gives precious data for signal identification [3].

1.2 Overview of DOA Estimation Techniques

The DOA performance is highly related with array geometry, antenna patterns, polarization and the chosen estimation algorithms Considering the operating frequency range of ESS, spiral and log-periodic antennas are preferred choices. These antennas are known as wideband antenna where their pattern performance is stable in terms of gain over the given frequency range. Especially spiral antennas radiate circularly polarized waves providing a significant benefit to detect linearly polarized target signals. Given the fact that ESS is operated in wide frequency range, the shortest inter-element distance of physically large antenna array possibly could not be designed to satisfy equal or less than $\lambda_{min}/2$ requirement, leading to ambiguous DOA estimation where λ_{min} the shortest wavelength is. On the other hand, achieving high DOA performance requires a larger array aperture. Therefore, to achieve high-accuracy direction-of-arrival (DOA) estimation, ambiguity

resolution techniques must be implemented using a specially designed array structure or mechanism.

There are two main methods used in DOA are the amplitude-comparison and phase-comparison or in another name interferometer. The phase comparison method offers greater accuracy, although at a higher cost compared to the amplitude comparison technique. While the typical DOA performance of amplitude comparison system ranges from 3 to 10 degrees RMS, the DOA performance of phase comparison system ranges from 0.1 to 3 degrees RMS [2]. In order to achieve unambiguous DOA estimation, antenna spacing should be equal or less than $\lambda_{min}/2$. The approximate RMS angular error in radians of the phase comparison is defined as

$$\sigma \approx \frac{\lambda \cos \varphi \sqrt{SNR}}{\pi d} \tag{1.1}$$

where, λ is wavelength, φ is the target angle, SNR is signal-to-noise ratio, d is the antenna spacing. In order to achieve 0.1 degrees RMS, SNR should be 50 dB for $\lambda/2$ element distance. This SNR level is rarely available so that array aperture should be increased. For instance, if the antenna spacing is expanded to16λ, then 20 dB SNR would be sufficient to achieve the same DOA performance. However, this adjustment introduces an ambiguity problem for 33 sectors within the 180-degree search angle. In order to solve the ambiguity, additional antenna elements located $\lambda/2$ distance could be assigned. This type of interferometers built in long baseline non-uniform-array structure are called multiple-baseline interferometers [2], shown in Figure 1.1.

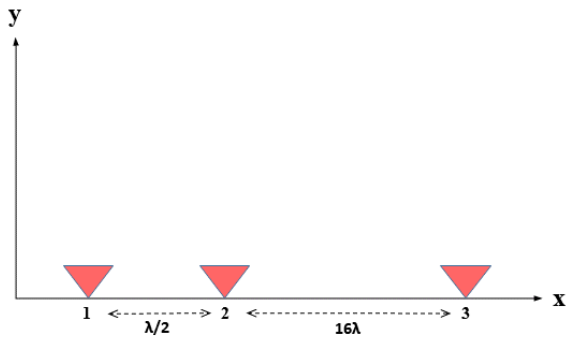

Figure 1.1. Multiply Base Line Interferometer

SODA (Second Order Difference Array) is the special case of multiple-baseline interferometer. It is the non-uniform long baseline linear array with three antennas shown in Figure 1.2. In SODA array design, Eqn. (1.2), Eqn. (1.3), and Eqn. (1.4) are satisfied.

$$d23 > d12 \gg \frac{\lambda_{min}}{2} \tag{1.2}$$

$$d23 - d12 = d_{\Delta} \tag{1.3}$$

$$\frac{\lambda_{min}}{2} \geq d_{\Delta} \tag{1.4}$$

where, d_{23} and d_{12} are the distances between antenna-2 and antenna-3, and between antenna-1 and antenna-2, respectively [4]. Comparing to multiple-baseline interferometer, SODA geometry does not require the $\lambda/2$ distance antenna spacing requirement, which is a significant advantage.

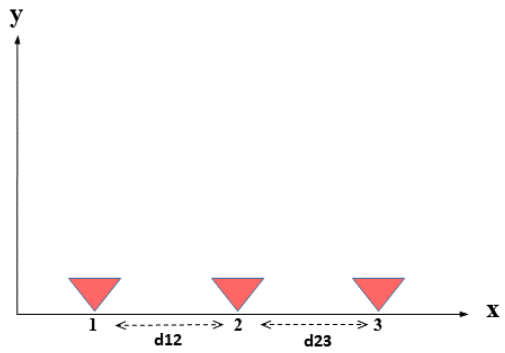

Figure 1.2. Soda Geometry

Amplitude comparison system does not require the antenna spacing to meet $\lambda_{min}/2$ requirement. As long as sufficient squint angles are maintained for the antennas, the inter-element distance does not affect the direction-of-arrival (DOA) performance. This provides ease of installation on several platforms. While phase comparison systems are operating at high accuracy but having possible ambiguity problem, additional amplitude comparison technique could be used in hybrid manner to perform course DOA estimation and eliminating ambiguity phenomena.

Rotatory mechanism can be implemented on interferometer array named as rotary interferometer [5] shown in Figure 1.3. The rotation axis is z plane with ω rotation frequency, interferometer is located in x-y plane, and φ-β are the DOA angles. This type of array is used in anti-radiation seeker technology for continuously rolling missiles. During rotation, additional spatial sampling points appear, allowing for the monitoring of the phase variation enabling to solve ambiguity. Furthermore, this spatial sampling process builds virtual planar circular array with two receiver channels providing two-dimensional DOA estimation.

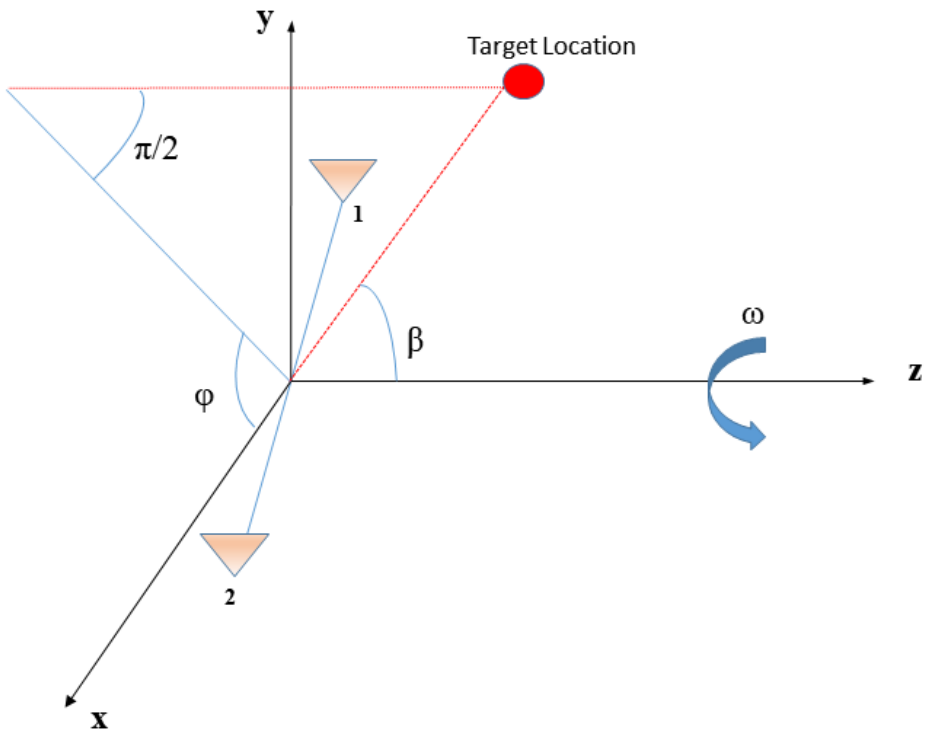

Figure 1.3. Rotary Interferometer

In array processing literature, there are well-known super resolution techniques such as MUSIC (Multiple Signal Classification) to achieve a high-performance DOA estimation. This method computes cross correlation matrix spectrum and perform an eigen-decomposition in order to obtain orthogonal the signal and noise subspace span vectors. However, the major drawback is to need high computational cost in real time applications required fast response [1].

1.3 Objective of the Thesis

This thesis aims to implement and develop ambiguity resolution algorithms for DOA estimation in long baseline arrays operated over a wideband frequency range. Several algorithms are investigated and developed on linear, planar, rotated and stationary designed arrays. Azimuth DOA estimation performances, under varying SNR, rotation information, array aperture etc. are examined in the given scenario. The Root Mean Square Error (RMSE) performance of all ambiguity resolution algorithms are evaluated through Monte Carlo simulations and compared with the Cramér-Rao Bound (CRB).

1.4 Outline of the Thesis

The organization of the thesis as follows: the diverse techniques for resolving angular ambiguity caused by spatial aliasing is defined, formulated and the DOA performance of these algorithms is analyzed under various scenario parameters in Chapter 2. In Chapter 3, the SODA planar array and the rotated SODA planar array are mathematically modeled, formulated, and investigated. The chapter defines these arrays and calculates their performance with respect to the Cramér-Rao bound. Additionally, it presents the Root Mean Square Error (RMSE) values to assess the accuracy of the performance metrics. In Chapter 4, the summary of all results is provided and some interpretations are made regarding the results.

CHAPTER 2

AMBUGITY RESOLUTION ALGORITHMS IN DIRECTION FINDING

In this chapter, DOA estimation techniques and ambiguity resolution algorithms are described, theoretically formulated and analyzed.

2.1 Amplitude Comparison Technique

The N-element linear array structure is considered as in Figure 2.1. The one RF target source is transmitted from an azimuth direction of φ. Every i antenna element, is squinted φ_i degrees for $i = 1,2 \ldots N$ in order to make an amplitude difference for receiver channels [6].

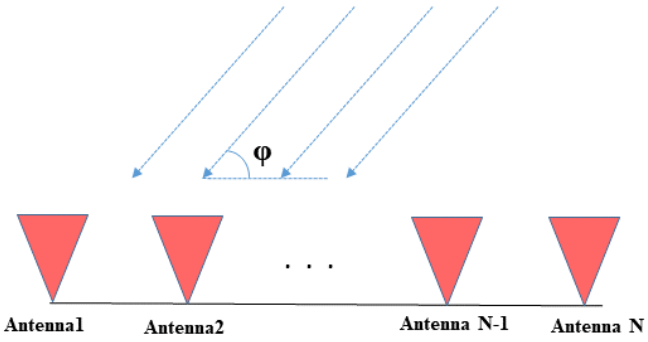

Figure 2.1. Linear Array Geometry

The receive signal model is given by [7]

$$S_i = AP_i(\varphi - \varphi_i) + n_i \tag{2.1}$$

where the S_i is the received signal amplitude, A is the source signal amplitude, P_i is the antenna voltage pattern, φ_i is the squint angle, n_i is the zero-mean independent additive white Gaussian noise with variance σ^2, for $i = 1,2 \ldots N$. DOA estimation of the azimuth angle, φ, is intended. The probability density function of noise is given as

$$f(x) = \frac{1}{\sqrt{2\pi\sigma^2}} e^{\frac{-x^2}{2\sigma^2}} \tag{2.2}$$

The joint probability density of observations is described as follows;

$$f(A, \varphi) = \prod_{i=1}^{N} \frac{1}{\sqrt{2\pi\sigma^2}} e^{\frac{-(S_i - AP_i(\varphi - \varphi_i))^2}{2\sigma^2}} \tag{2.3}$$

The maximum likelihood estimation $\hat{\varphi}$ of φ, maximizes the density function given in Eqn. (2.3) as defined in Eqn. (2.4) and Eqn. (2.5) respectively;

$$\hat{\varphi} = argmax_{\varphi}(f(A, \varphi)) \tag{2.4}$$

The maximum likelihood estimation $\hat{\varphi}$ of φ can be written, as the minimization of negative logarithm of Eqn. (2.3) with eliminating constants, given in Eqn. (2.5). Log-likelihood estimation is defined in Eqn. (2.6).

$$J(A, \varphi) = \sum_{i=1}^{N} (S_i - AP_i(\varphi - \varphi_i))^2 \tag{2.5}$$

$$\hat{\varphi} = argmin_{\varphi}(J(A, \varphi)) \tag{2.6}$$

The log-likelihood function consists of φ and A terms. In order to estimate φ, the estimation of A, should be found described in Eqn. (2.7).

$$\hat{A} = argmin_{\mathrm{A}}(J(A, \varphi)) \tag{2.7}$$

Taking derivate of Eqn. (2.5) with respect to A, setting to zero and solving for A, gives $\hat{A}$ as in Eqn. (2.8) and Eqn. (2.9).

$$\frac{dJ(A, \varphi)}{dA} = \sum_{i=1}^{N} (-2S_i P_i(\varphi - \varphi_i) + 2AP_i{}^2(\varphi - \varphi_i)) = 0 \tag{2.8}$$

$$\widehat{A_{ML}} = \frac{\sum_{i=1}^{N} (S_i P_i(\varphi - \varphi_i))}{\sum_{i=1}^{N} P_i{}^2(\varphi - \varphi_i)} \tag{2.9}$$

Substituting Eqn. (2.9) in Eqn. (2.6) results in Eqn. (2.10) and Eqn. (2.11), respectively.

$$\hat{\varphi} = argmin_{\varphi}(\sum_{i=1}^{N}(S_i - \frac{\sum_{i=1}^{N}(S_i P_i(\varphi - \varphi_i))}{\sum_{i=1}^{N} {P_i}^2(\varphi - \varphi_i)} P_i(\varphi - \varphi_i))^2) \quad (2.10)$$

$$\hat{\varphi} = argmin_{\varphi}(\sum_{i=1}^{N} {S_i}^2 - \frac{(\sum_{i=1}^{N} S_i P_i(\varphi - \varphi_i))^2}{\sum_{i=1}^{N} {P_i}^2(\varphi - \varphi_i)}) \quad (2.11)$$

The term of $\sum_{i=1}^{N} {S_i}^2$ doesn't contain any expressions of φ that affects minimization in the Eqn. (2.11). Hence, the simplified version of Eqn. (2.11) becomes a maximization of the log-likelihood function given in Eqn. (2.12)

$$\widehat{\varphi_{ML}} = argmax_{\varphi}(\frac{(\sum_{i=1}^{N} S_i P_i(\varphi - \varphi_i))^2}{\sum_{i=1}^{N} {P_i}^2(\varphi - \varphi_i)}) \quad (2.12)$$

2.2 Phase Comparison Technique

The two-element interferometer array [8] is designed as in Figure 2.2.

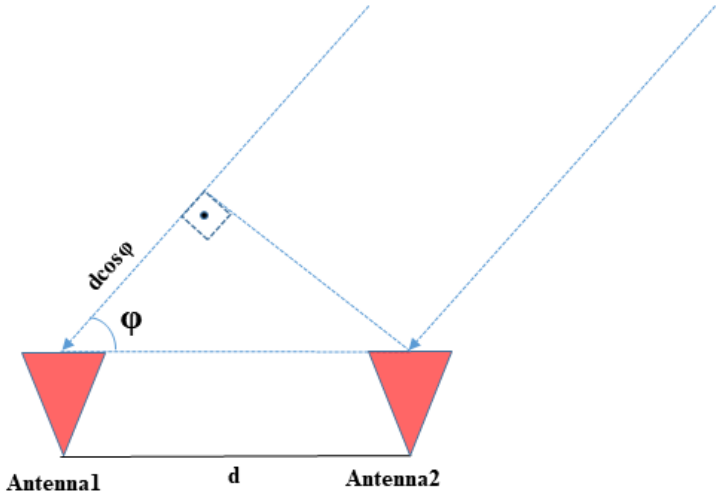

Figure 2.2. Phase Comparison Technique

The received signal models $s_1(t)$ and $s_2(t)$ for antenna-1 and antenna-2, respectively is given [9] in Eqn. (2.13) and Eqn. (2.14)

$$s_1(t) = cos\big(2\pi f_{RF}(t + \Delta t)) + n_{1(t)}\big) \tag{2.13}$$

$$s_2(t) = cos\big(2\pi f_{RF}(t)) + n_{2(t)}\big) \tag{2.14}$$

where f_{RF} is the source frequency, Δt is the time delay between antennas, $n_{1(t)}$ and $n_{2(t)}$ are zero-mean independent additive white Gaussian noise signals. Time delay is calculated in Eqn. (2.15)

$$\Delta t = \frac{d\cos\varphi}{c} \tag{2.15}$$

where d is the inter-element distance, c is the speed of light. Phase difference $\Delta\psi$, is defined in Eqn. (2.16) and Eqn.(2.17)

$$\Delta\psi = 2\pi f_{RF}\Delta t \tag{2.16}$$

$$\Delta\psi = 2\pi f_{RF}\frac{d\cos\varphi}{c} \tag{2.17}$$

The DOA estimation of φ, is given in Eqn. (2.18)

$$\hat{\varphi} = a\cos\left(\frac{c\Delta\psi}{2\pi f_{RF}d}\right) \tag{2.18}$$

The maximum likelihood estimation of the phase difference and DOA φ, $\Delta\psi$ are given respectively [4] in Eqn. (2.19) and Eqn. (2.20)

$$\widehat{\Delta\psi_{ML}} = angle(\boldsymbol{s_2}(f_{RF})\boldsymbol{s_1}^*(f_{RF})) \tag{2.19}$$

$$\widehat{\varphi_{ML}} = a\cos\left(\frac{\widehat{\Delta\psi_{ML}} * c}{2 * \pi * f_{RF} * d}\right) \tag{2.20}$$

where $\boldsymbol{s_2}(f_{RF})$ and $\boldsymbol{s_1}(f_{RF})$ are the fourier transforms of $s_1(t)$ and $s_2(t)$ at the frequency f_{RF} [10].

2.2.1 Phase Ambiguity Phenomenon

As mentioned earlier, the DOA estimation becomes ambiguous when antenna spacing exceeds $\lambda/2$, due to phase wrapping within the search sector. The ambiguity problem can be mathematically defined as follows:

Recall the phase difference between two antennas $\Delta\psi$ is defined as

$$\Delta\psi = 2\pi f_{RF} \frac{d \cos\varphi}{c} \tag{2.21}$$

The maximum and minimum of the phase difference are observed when source is located at $\varphi = 0^{\circ}$ and $\varphi = 180^{\circ}$. So, the phase difference is bounded by

$$-2\pi f_{RF} \frac{d}{c} \leq \Delta\psi \leq 2\pi f_{RF} \frac{d}{c} \tag{2.22}$$

To obtain an unambiguous phase difference and estimate the direction of arrival (DOA) angle unambiguously, all potential phase differences resulting from the source's location must fall within the interval $[-\pi, \pi]$. Therefore, antenna spacing d must be satisfied the following equation;

$$d \leq \frac{c}{2f_{RF}} = \frac{\lambda}{2} \tag{2.23}$$

For the long-baseline arrays where $d > \lambda/2$, the unambiguous phase difference will exceed the range $[-\pi, \pi]$ described as

$$\widehat{\Delta\boldsymbol{\psi}}_{\mathbf{ambiguous}} = \widehat{\Delta\psi}_{measured} + 2\pi p \tag{2.24}$$

where $\widehat{\Delta\psi}_{measured}$ is the measured ambiguous phase difference, p is the integer representing the ambiguity number associated with one of the possible 2π phase differences of the measured phase difference. From Eqn. (2.22) and Eqn.(2.24) , p is bounded by

$$\left\lceil -\frac{f_{RF}d}{c} - \frac{\widehat{\Delta\psi}_{measured}}{2pi} \right\rceil \leq p \leq \left\lfloor \frac{f_{RF}d}{c} - \frac{\widehat{\Delta\psi}_{measured}}{2pi} \right\rfloor \tag{2.25}$$

where operators ⌈ ⌉ and ⌊ ⌋ denote the ceiling and floor functions, respectively and $\widehat{\Delta\psi}_{measured}$ is in the $[-\pi, \pi]$ interval. Upper bound for Eqn. (2.25) can be written as

$$-round\left(\frac{f_{RF}d}{c}\right) \leq p \leq round\left(\frac{f_{RF}d}{c}\right) \tag{2.26}$$

The total maximum number of ambiguities, N, can be defined as

$$k = round\left(\frac{f_{RF}d}{c}\right) \tag{2.27}$$

$$N = 2k + 1 \tag{2.28}$$

Using Eqn. (2.18), Eqn. (2.24), Eqn. (2.26) and Eqn. (2.28), the corresponding ambiguous DOA estimation angles can be written as

$$\widehat{\Delta\boldsymbol{\psi}}_{\mathbf{ambiguous}}: \{\widehat{\Delta\psi}_1, \widehat{\Delta\psi}_2 \dots, \widehat{\Delta\psi}_{2k+1}\} = \widehat{\Delta\psi}_{measured} \pm 2\pi p \tag{2.29}$$

$$\widehat{\boldsymbol{\varphi}} = a\cos\left(\frac{\widehat{\Delta\boldsymbol{\psi}}_{\mathbf{ambiguous}} c}{2\pi f_{RF} d}\right) \tag{2.30}$$

$$\hat{\varphi}(p) = a\cos\left(\frac{(\widehat{\Delta\psi}_{measured} + 2\pi p)c}{2\pi f_{RF} d}\right) \tag{2.31}$$

Two cases such as $d = \lambda$ with two phase-wrapping and $d = 2\lambda$ with four phase-wrapping over full azimuth scan are shown in Figure 2.3 and Figure 2.4.

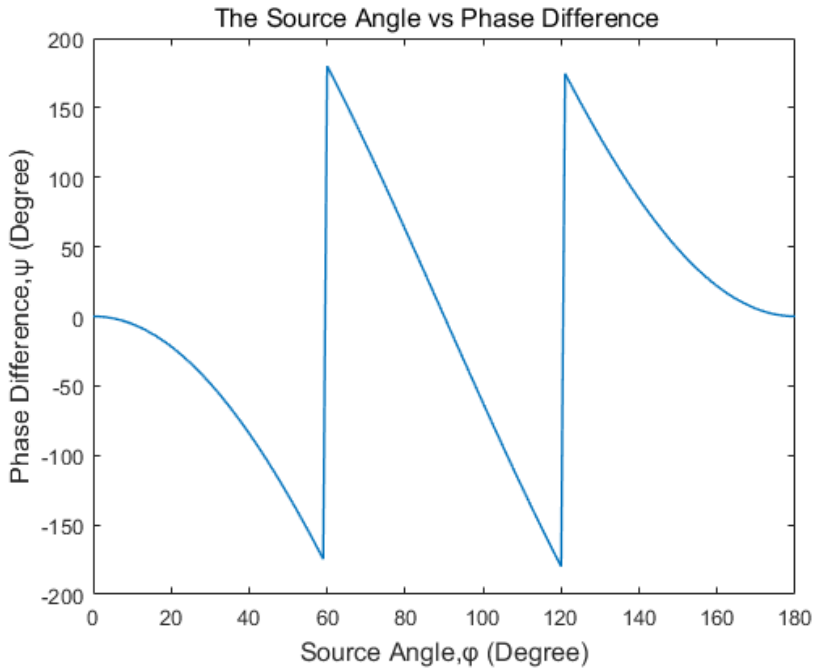

Figure 2.3. $d = \lambda$

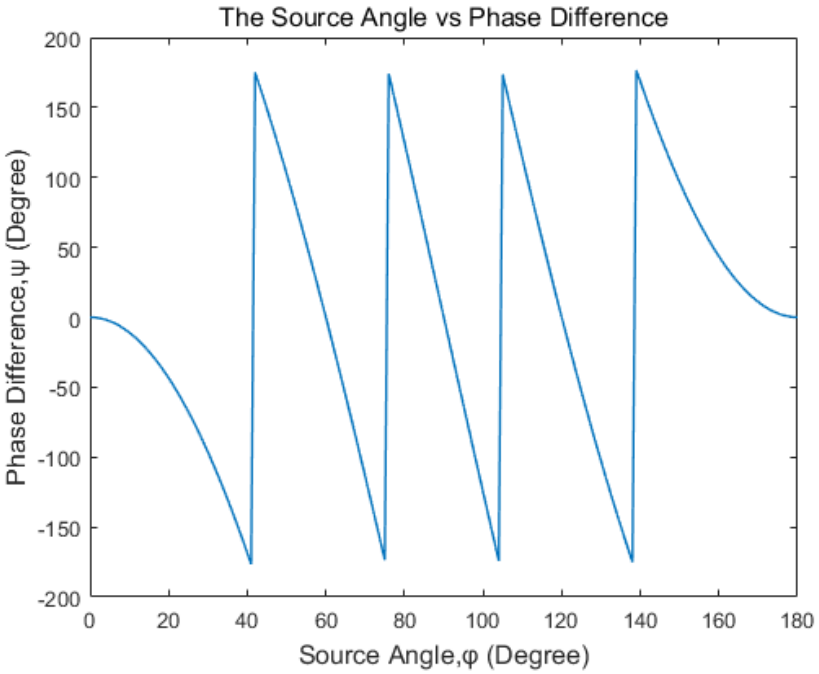

Figure 2.4. $d = 2\lambda$

Consider a long baseline interferometer with $d = 2\lambda$, $f_{RF} = 18\ GHz$ and the source angle is $\varphi = 120^{\circ}$. Eqn. (2.21) gives the unambiguous phase difference as

$$\Delta\psi = -362.011° \tag{2.32}$$

The measured ambiguous phase difference is

$$\widehat{\Delta\psi}_{measured} = [\Delta\psi]_{2\pi} = -2.011° \tag{2.33}$$

The set of ambiguity numbers is computed from Eqn. (2.25) as

$$\left\lceil -\frac{f_{RF}d}{c} - \frac{\widehat{\Delta\psi}_{measured}}{2pi} \right\rceil \leq p \leq \left\lfloor \frac{f_{RF}d}{c} - \frac{\widehat{\Delta\psi}_{measured}}{2pi} \right\rfloor \quad (2.34)$$

$$-1 \leq p \leq 2 \quad (2.35)$$

Then the resultant corresponding ambiguous DOA estimation angles can be calculated from Eqn. (2.31) as

$$\hat{\varphi}(p) = \{\, 120^{\circ}, 90.159^{\circ}, 60.367^{\circ}, 7.402^{\circ}\} \quad (2.36)$$

2.3 Amplitude and Phase Comparison Hybrid Technique

In order to resolve the ambiguity problem, amplitude comparison can be implemented in addition to phase comparison [11]. Amplitude comparison DOA estimation is less accurate and coarse however enables to resolve the ambiguity. Consider the array in Figure 2.1 with two elements. Ambiguity resolution algorithm flows as follows [12];

i. Perform Fourier Transform on detected $s_1(t)$ and $s_2(t)$
ii. Perform the frequency estimation by finding the peak of spectrum, $\widehat{f_{RF}}$
iii. Find the phase of the detected signals at the estimated frequency
iv. Perform the Phase Comparison in order to find phase difference $\widehat{\Delta\boldsymbol{\psi}}_{\mathbf{MLambiguous}}$

The above steps are shown in Figure 2.5

v. Find magnitudes of the detected signals at the estimated frequency
vi. Perform the Amplitude Comparison in order to find $\widehat{\boldsymbol{\varphi}}_{\mathbf{MLcourse}}$

The above steps are shown in Figure 2.6.

vii. Find all possible ambiguous phase difference values, $\{\widehat{\Delta\psi}_1, \widehat{\Delta\psi}_2 \ldots, \widehat{\Delta\psi}_{2k+1}\}$

viii. Find all possible DOA angles, $\{\hat{\varphi}_{ML_1}, \hat{\varphi}_{ML_2} \dots, \hat{\varphi}_{ML_{2K+1}}\}$

ix. Compare $\{\hat{\varphi}_{ML_1}, \hat{\varphi}_{ML_2} \dots, \hat{\varphi}_{ML_{2K+1}}\}$ with $\hat{\boldsymbol{\varphi}}_{\mathbf{MLcourse}}$, and find the closest

x. Find the unambiguous angle, $\hat{\boldsymbol{\varphi}}_{\mathbf{MLfinal}}$

The above steps are shown in Figure 2.7

Figure 2.5. Phase Comparison Block

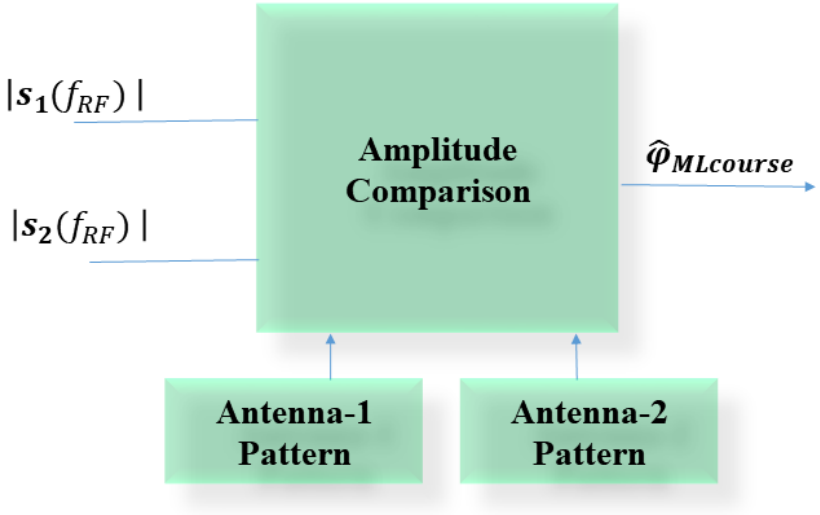

Figure 2.6. Amplitude Comparison Block

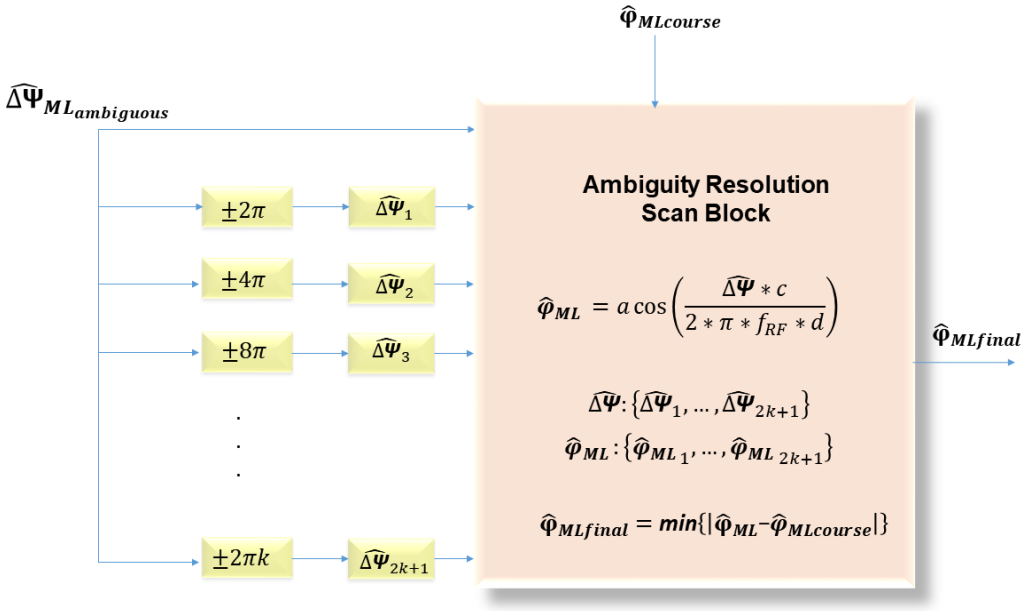

Figure 2.7. Ambiguity Resolution Scan Block

2.3.1 Amplitude and Phase Comparison Hybrid Technique Simulation Results

Consider two-element interferometry is given in Figure 2.2. The simulation parameters are given in Table 2.1.

Table 2.1 Simulation Parameters

Parameter	*Value*
Frequency	18 GHz
SNR	20 dB, 0 dB
Search Angle	$60^{\circ} < \varphi < 120^{\circ}$
Scan Angle	0.1°
Sampling Frequency	125 MHz
Number of Trials	10
Number of Snapshots	125
Antenna Spacing	7.75λ
Antenna Pattern Type	Gaussian
Antenna 3dB Beamwidth	45°
Antenna Tilt Angle	15°

The antennas are physically tilted 15° from their standard orientation. Their radiation patterns are given in Figure 2.8. The search is constrained to $60^{\circ} < \varphi < 120^{\circ}$. Because the difference in antenna patterns exhibits a steep curve within this range, which enhances the performance of the amplitude comparison algorithm.

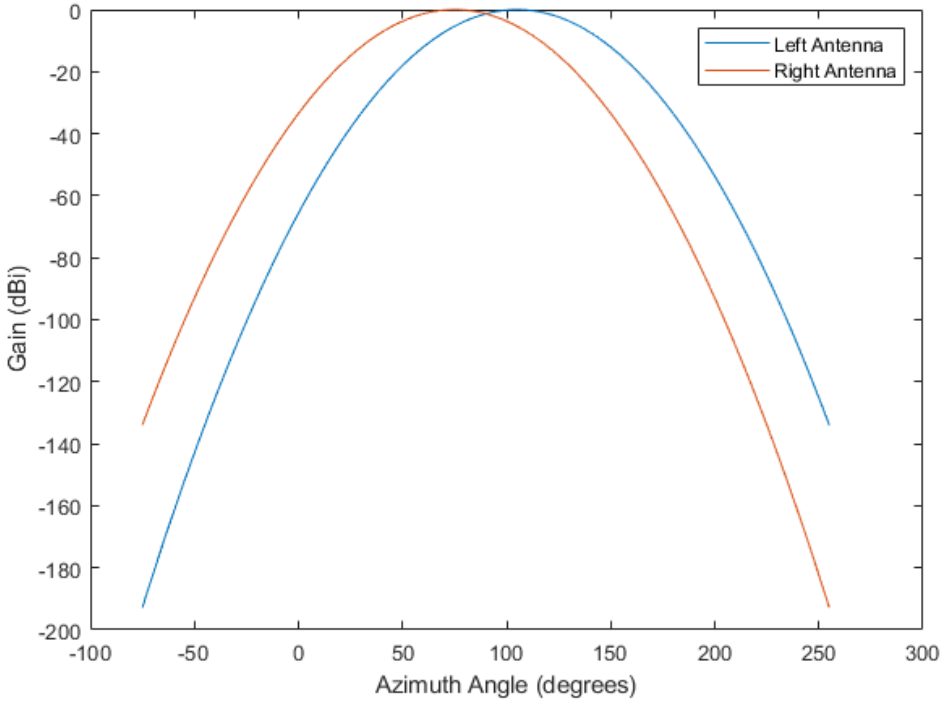

Figure 2.8. The Patterns of the Left and Right Antennas

The performance of the algorithm is shown in Figure 2.9 and Figure 2.10. The Amplitude-Phase Comparison Hybrid Method is a valuable approach for rapidly resolving ambiguities and maintaining low computational complexity. While it provides an efficient means of addressing ambiguities, the accuracy of the amplitude comparison can sometimes constrain the overall performance of the system. This trade-off between ambiguity resolution speed and precision is a key consideration, as the method's primary strength lies in its ability to quickly and efficiently solve ambiguities, potentially at the expense of some level of accuracy in amplitude-based measurements.

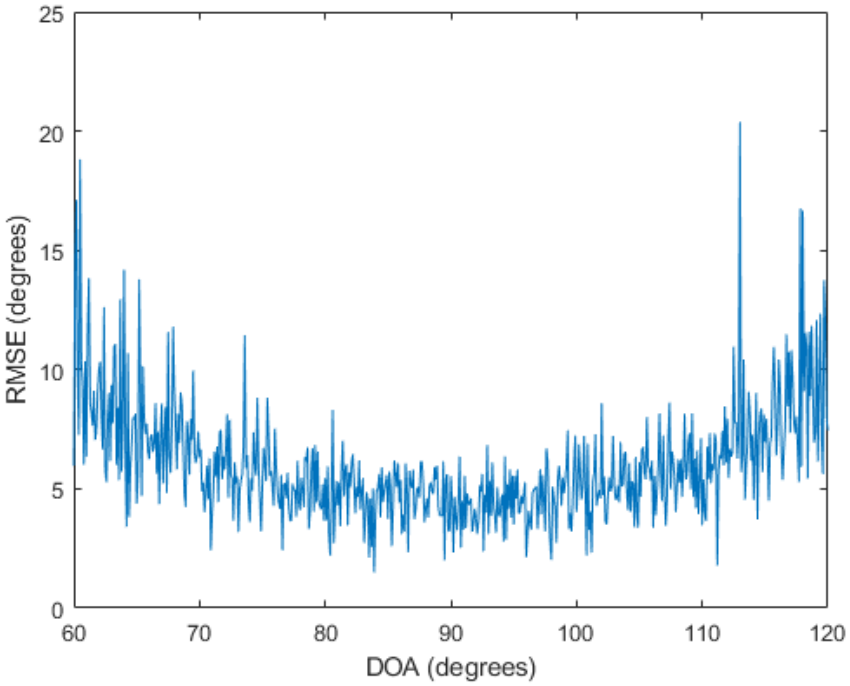

Figure 2.9. SNR=0 dB

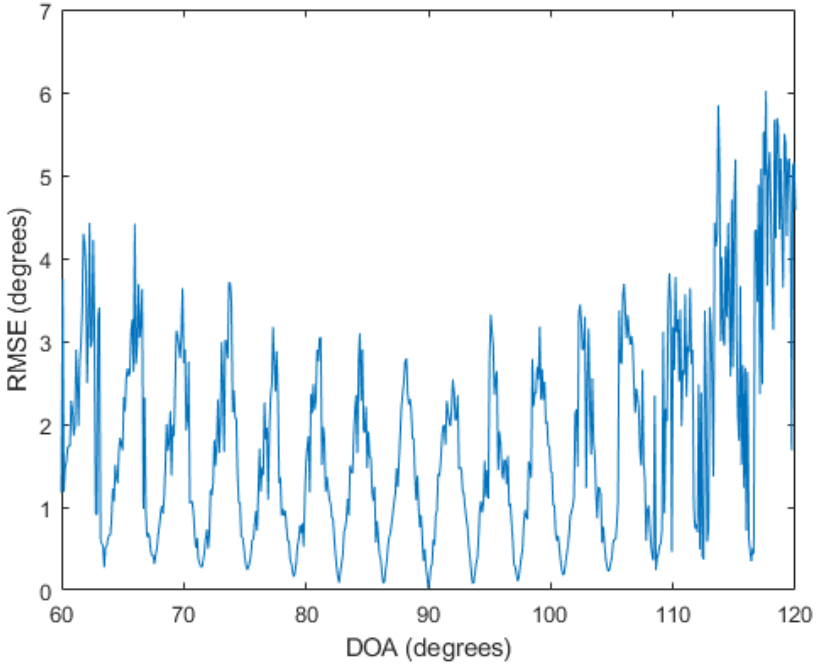

Figure 2.10. SNR= 20 dB

2.4 Amplitude Comparison and MUSIC Hybrid Technique

While MUSIC algorithm [13] is a super resolution algorithm which offers high accuracy and resolution in DOA estimation, it still encounters issues with ambiguity. In order to overcome these issues, amplitude comparison method can be utilized. The received signal model is defined as;

$$y(t) = As(t) + e(t) \tag{2.37}$$

Where A is the steering matrix, $e(t)$ is zero-mean independent additive white Gaussian noise. Sample covariance matrix is calculated as;

$$\hat{R}_y = \frac{1}{N}\sum_{t=1}^{N} y(t)y(t)^H \tag{2.38}$$

After performing singular value decomposition (SVD), eigenvectors of noise subspace are found. MUSIC pseudo spectrum is given as;

$$p(\varphi) = \frac{1}{a^H(\varphi)GG^Ha(\varphi)} \tag{2.39}$$

where φ is the search angle, G represents the noise subspace vectors.

Ambiguity resolution algorithm flows as follows;

i. Perform Fourier Transform on detected $s_1(t)$ and $s_2(t)$
ii. Perform the frequency estimation by finding the peak of spectrum, $\widehat{f_{RF}}$
iii. Find magnitudes of the detected signals at the estimated frequency

iv. Perform the Amplitude Comparison in order to find $\hat{\boldsymbol{\varphi}}_{\mathbf{MLcourse}}$

v. Calculate the sample covariance matrix, $\hat{R}_y$

vi. Perform the SVD on $\hat{R}_y$

vii. Find the noise space vectors and construct MUSIC pseudo spectrum

viii. Find all peaks in the spectrum corresponding to possible ambiguous DOA angles, $\{\hat{\varphi}_{MUSIC_1}, \hat{\varphi}_{MUSIC_2} \cdots, \hat{\varphi}_{MUSIC_K}\}$

ix. Compare $\{\hat{\varphi}_{MUSIC_1}, \hat{\varphi}_{MUSIC_2} \cdots, \hat{\varphi}_{MUSIC_K}\}$ with $\hat{\boldsymbol{\varphi}}_{\mathbf{MLcourse}}$, and find the closest

x. Find the unambiguous angle, $\hat{\boldsymbol{\varphi}}_{\mathbf{MUSICfinal}}$

2.4.1 Amplitude Comparison and MUSIC Hybrid Technique Simulation Results

Consider two-element interferometry is given in Figure 2.2. The simulation parameters are given in Table 2.2.

Table 2.2 Simulation Parameters

Parameter	*Value*
Frequency	18 GHz
SNR	20 dB, 0 dB
Search Angle	$60^{\circ} < \varphi < 120^{\circ}$
Scan Angle	0.1°
Sampling Frequency	125 MHz
Number of Trials	10
Number of Snapshots	125
Antenna Spacing	7.75λ
Antenna Pattern Type	Gaussian
Antenna 3dB Beamwidth	45°
Antenna Tilt Angle	15°

The type, specifications, and setup of the antennas are identical to those outlined in Section 2.3.1

The performance of the algorithm is given in Figure 2.11 and Figure 2.12. By utilizing the super-resolution algorithm MUSIC, the accuracy of the amplitude comparison method is enhanced. However, the inherent limitations of the amplitude comparison method still lead to subpar performance, which impacts the overall effectiveness of the system, albeit at the cost of increased complexity in resolving ambiguities.

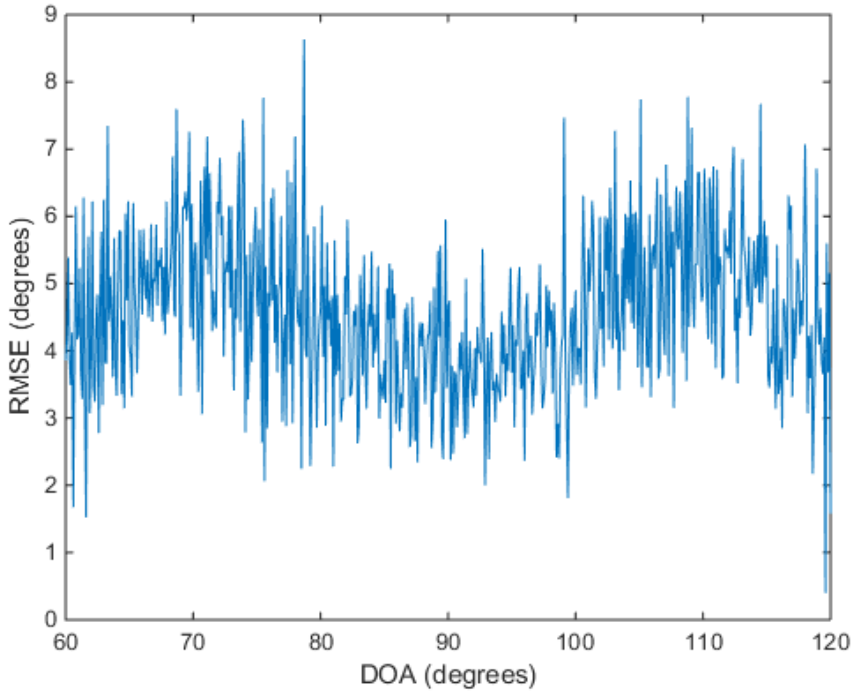

Figure 2.11. SNR= 0 dB

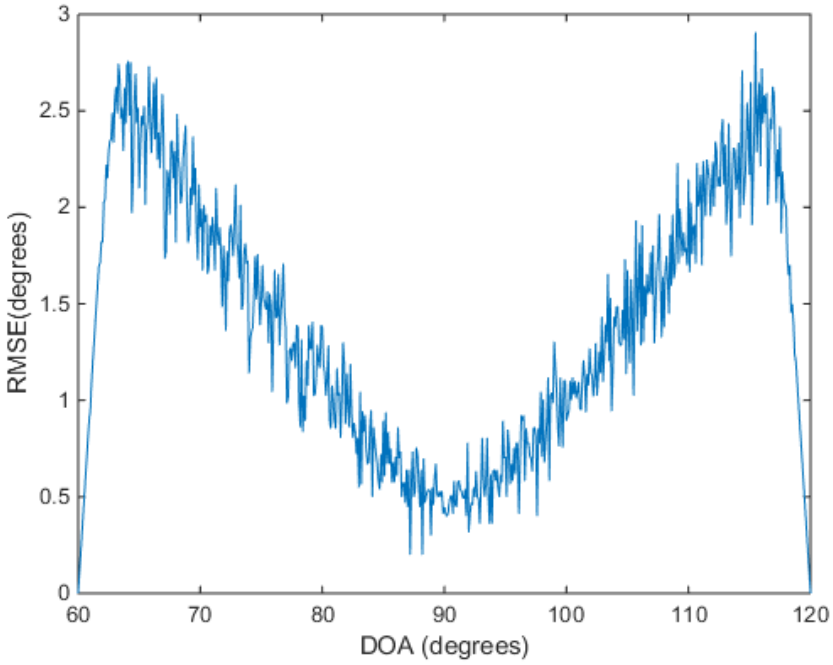

Figure 2.12. SNR= 20 dB

2.5 Rotary Interferometer

Rotary or rotating interferometer is shown in Figure 2.13. The array is continuously rolling in x-y plane. The rotation frequency is ω, the rotation axis is z plane, φ-β are the DOA angles of the source [5] [14] [15].

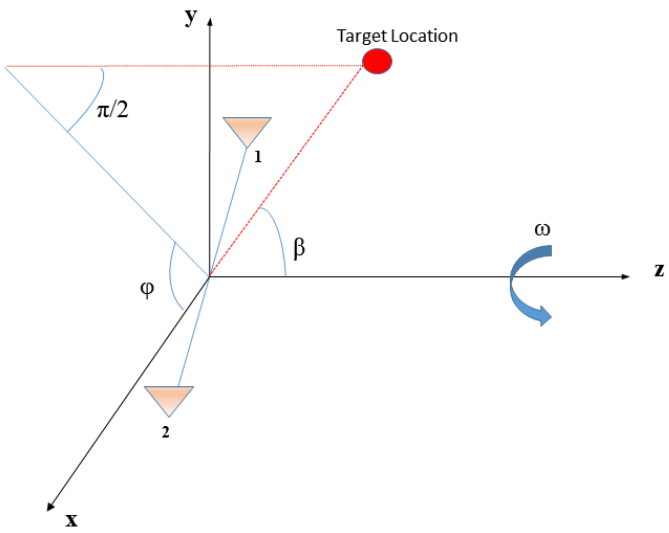

Figure 2.13. Rotating Interferometry

The relationship of phase difference between two antennas is given as:

$$\alpha(n) = \frac{2\pi d}{\lambda} \sin\beta \cos(\omega \Delta t(n-1) + \varphi) \tag{2.40}$$

where Δt is the sampling interval or pulse repetition interval, n is the pulse number from 1 to N, φ , β are the azimuth and elevation angle of the source and estimation of $\alpha(n)$, $\hat{\alpha}(n) \in (-\pi, \pi)$. In order to obtain $\alpha(n)$ unambiguously, the integrator $c(n)$ is utilized as;

$$c(n) = \alpha(n) - \hat{\alpha}(n) \tag{2.41}$$

$$c(n) = 2\pi k \tag{2.42}$$

where k is an integer value and $\alpha(n)$ has the cycle ambiguity.

Rotating interferometry employs an integrator to execute a phase accumulation sequence for eliminating phase ambiguity. The accumulated phase is then adjusted using the following procedure;

$$\hat{c}(1) = 0 \tag{2.43}$$

$$\hat{c}(n) = \hat{c}(n-1) + 2\pi, \qquad \hat{\alpha}(n) - \hat{\alpha}\,(n-1) < -\pi \tag{2.44}$$

$$\hat{c}(n) = \hat{c}(n-1) - 2\pi, \qquad \hat{\alpha}(n) - \hat{\alpha}\,(n-1) > -\pi \tag{2.45}$$

$$\hat{c}(n) = \hat{c}(n-1), \qquad otherwise \tag{2.46}$$

Also amended phase, $\hat{\alpha}_c(n)$, is defined as;

$$c(n) = \hat{c}(n) + U \tag{2.47}$$

$$\hat{\alpha}_c(n) = \hat{\alpha}(n) + \hat{c}(n) \tag{2.48}$$

where U is the bias term. $\hat{\alpha}_c(n)$, is in the sinusoidal form seen in Eqn. (2.40), such as

$$y(t) = Acos(\omega t) + Bsin(\omega t) + D \tag{2.49}$$

Three parameters of least square estimate for A, B and D is done to estimate amplitude, initial phase and bias of $\hat{\alpha}_c(n)$. $y_i(i = 1,2, \dots n)$ is the amended phase difference at the time t_i. We have to minimize following equation

$$\varepsilon = \sum_{i=}^{n} [y_i - Acos(\omega t) - Bsin(\omega t) - D]^2 \tag{2.50}$$

To estimate A, B and D, following matrix is constructed

$$\psi = \begin{pmatrix} \cos(\omega t_1) & \sin(\omega t_1) & 1 \\ \vdots & \vdots & \vdots \\ \cos(\omega t_n) & \sin(\omega t_n) & 1 \end{pmatrix} \tag{2.51}$$

$$y = \begin{bmatrix} y_1 \\ \vdots \\ y_n \end{bmatrix} \tag{2.52}$$

$$x = \begin{bmatrix} A \\ B \\ D \end{bmatrix} \tag{2.53}$$

where ω is the rotation frequency. Eqn.(2.51) can be written as

$$\varepsilon = (y - \psi x)^T (y - \psi x) \tag{2.54}$$

The least square solution of x can be written as

$$\hat{x} = (\psi^T \psi)^{-1}(\psi^T y) \tag{2.55}$$

The fitting function can be defined as

$$\hat{\boldsymbol{y}}_i = Acos(\omega t_i) + Bcos(\omega t_i) + D \tag{2.56}$$

$$\hat{\boldsymbol{y}}_i = Ccos(\omega t_i + \varphi) + D \tag{2.57}$$

where $C = \sqrt{A^2 + B^2}$

$$\hat{\varphi} = tan^{-1}\left|\frac{-B}{A}\right|, \qquad A \geq 0 \tag{2.58}$$

$$\hat{\varphi} = tan^{-1}\left|\frac{-B}{A}\right| + \pi, \qquad A < 0 \tag{2.59}$$

where $\hat{\varphi}$ is the DOA estimation of the source signal.

2.5.1 Rotary Interferometer Simulation Results

For two-element rotating interferometry is given in Figure 2.13. The simulation parameters are given in Table 2.3

Table 2.3 Simulation Parameters

Parameter	*Value*
Frequency	18 GHz
SNR	20 dB, 0 dB
Search Angle	$0^{\circ} < \varphi < 180^{\circ}$
Scan Angle	0.1°
Sampling Frequency	125 MHz
Number of Trials	10
Number of Snapshots	125
Antenna Spacing	7.75λ
Revolution Frequency (f_r)	7,5, 10 Hz
Processed Number of Pulse	75, 100

The performance of the algorithm is presented in Figure 2.14, Figure 2.15, Figure 2.16 and Figure 2.17 . Due to its rotation, interferometry exhibits an isometric response and very good accuracy. However, its performance is highly dependent on the illumination of the source signal. When the number of pulses used is reduced, or if the source has a high pulse repetition interval, the performance degrades significantly.

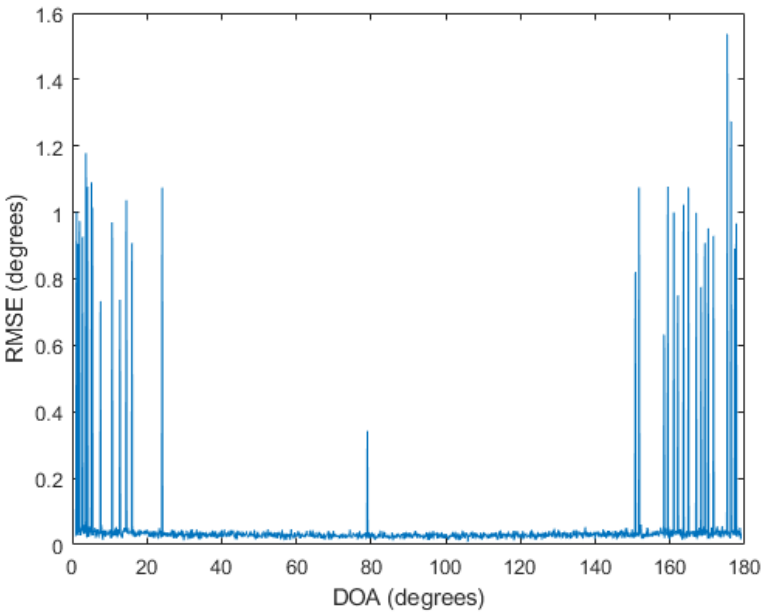

Figure 2.14. SNR= 0 dB, f_r = 100 Hz

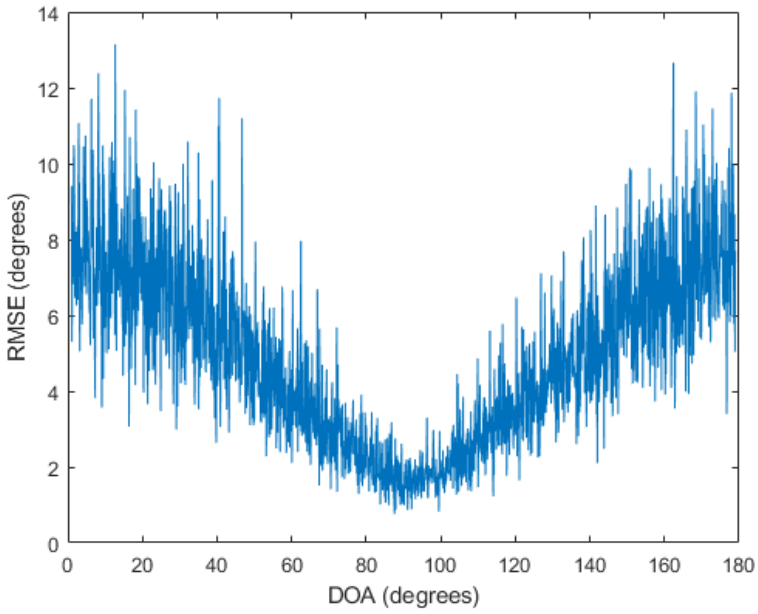

Figure 2.15. SNR= 0 dB, f_r = 75 Hz

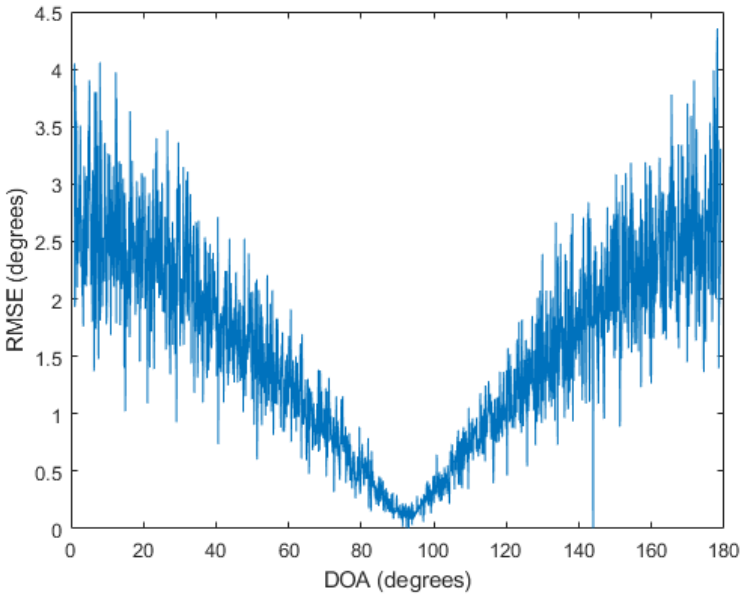

Figure 2.16. SNR= 20 dB, f_r = 75 Hz

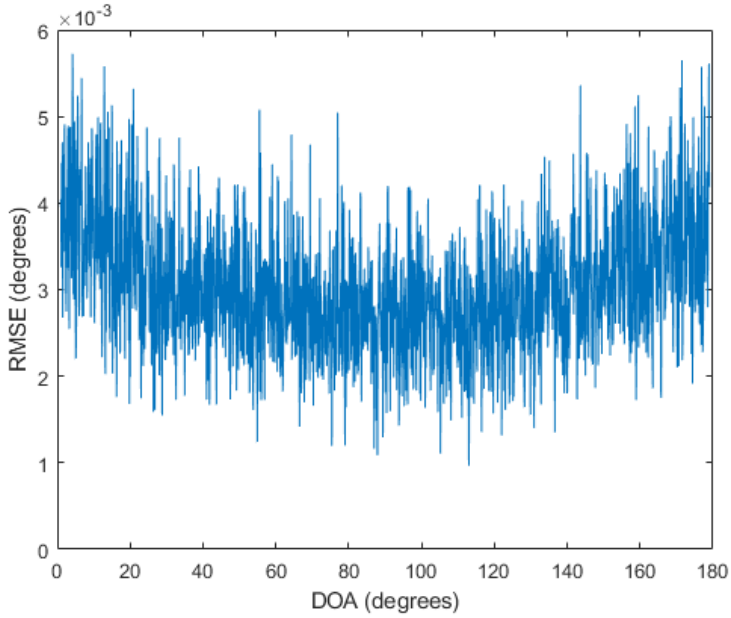

Figure 2.17. SNR= 20 dB, f_r = 100 Hz

2.6 SODA Interferometer

SODA geometry is given in Figure 2.18 [4] [16] [17]. The SODA array requires a minimum of three antenna elements.

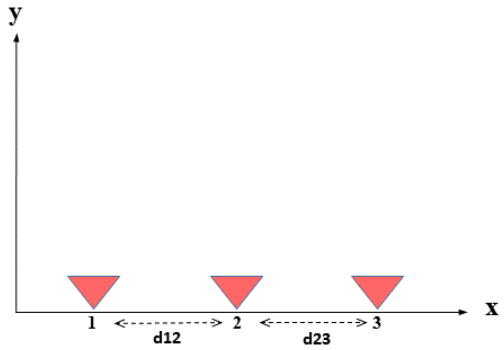

Figure 2.18. Linear SODA Array

Phase differences between antenna couples are written as;

$$\psi_{12} = \frac{2\pi f d_{12}}{c} \cos\varphi \tag{2.60}$$

$$\psi_{23} = \frac{2\pi f d_{23}}{c} \cos\varphi \tag{2.61}$$

The antenna distances are defined as;

$$d_{23} > d_{12} \gg \frac{\lambda_{min}}{2} \tag{2.62}$$

$$d_{23} - d_{12} = d_{\Delta} \tag{2.63}$$

$$\frac{\lambda_{min}}{2} \geq d_{\Delta} \tag{2.64}$$

The second order phase delay is given as;

$$\psi_{\Delta} = \psi_{23} - \psi_{12} \tag{2.65}$$

$$\psi_{\Delta} = \frac{2\pi f(d_{23} - d_{12})}{c} \cos\varphi \tag{2.66}$$

$$\psi_{\Delta} = \frac{2\pi f(d_{\Delta})}{c} \cos\varphi \tag{2.67}$$

$$\psi_{\Delta} = \cos^{-1} \frac{c\psi_{\Delta}}{2\pi f d_{\Delta}} \tag{2.68}$$

The unambiguous DOA estimation is achieved using the designed SODA array, along with a virtual array consisting of two elements spaced by $d_{\Delta} \leq \frac{\lambda_{min}}{2}$ spacing.

2.6.1 SODA Interferometer Simulation Results

For the given array in Figure 2.18, the simulation is performed according to Table 2.4.

Table 2.4 Simulation Parameters

Parameter	*Value*
Frequency	18 GHz
SNR	20 dB, 0 dB
Search Angle	$40^{\circ} < \varphi < 140^{\circ}$
Scan Angle	0.1°
Sampling Frequency	125 MHz
Number of Trials	10
Number of Snapshots	125
Total Antenna Aperture	7.75λ

Due to the linear array structure of the SODA array, its performance degrades at the end-fire points of the array. Therefore, the search is constrained to $40^{\circ} < \varphi < 140^{\circ}$ which provides a clearer indication of the SODA array's performance. The performance of the SODA array is presented in Figure 2.19 and Figure 2.20. The SODA array is presented the robust ambiguity resolution however due to short-baseline virtual array characteristics, the DOA performance is limited. Therefore, additional technique has to be applied such as SODA-Based Inference (SBI) or MUSIC [4]. The SODA array offers robust ambiguity resolution; however, its performance is limited by the characteristics of the short-line virtual array. Therefore, additional techniques, such as SODA-Based Inference (SBI) or MUSIC, need to be applied to enhance performance.

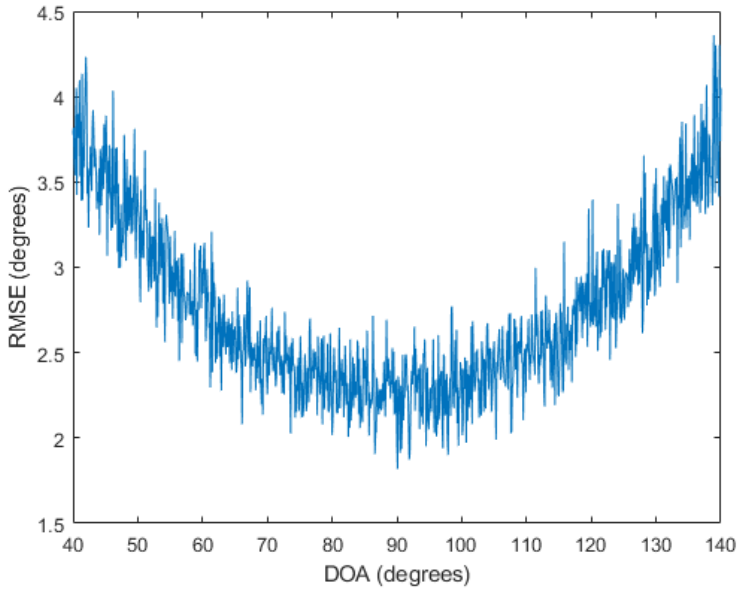

Figure 2.19. SNR=0dB

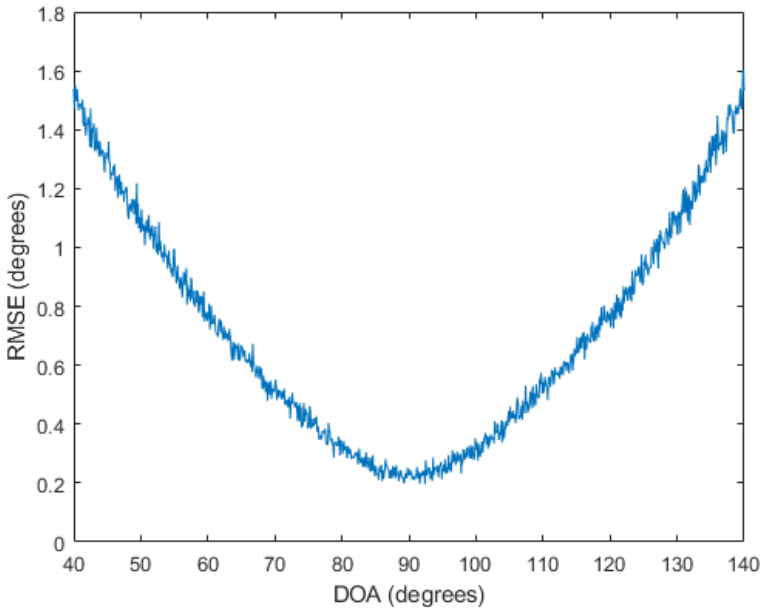

Figure 2.20. SNR=20dB

2.7 Comparison of the Ambiguity Resolution Algorithms

Overall comparison is shown in Figure 2.21. All simulations are performed according to parameters in Table 2.5.

Table 2.5 Simulation Parameters

Parameter	*Value*
Frequency	18 GHz
SNR	20 dB
Search Angle	$60^{\circ} < \varphi < 120^{\circ}$
Scan Angle	0.1°
Sampling Frequency	125 MHz
Number of Trials	10
Number of Snapshots	125
Total Antenna Aperture	7.75λ

Amplitude comparison provides relatively poor performance and a narrow field of view but has low computational complexity. Its performance can be improved with the use of super-resolution algorithms. Rotating interferometers offer the best accuracy with an isometric response, but their robustness is relatively poor, heavily depending on the source signal parameters. The SODA array delivers moderate performance and is affected by end-fire angles due to its short-line linear array behavior. However, it demonstrates good robustness. To enhance the performance of the SODA array, additional algorithms such as SODA-Based Inference (SBI) [18] or MUSIC can be implemented. Hence, throughout this thesis, particular emphasis is placed on the rotated SODA array structure, which offers not only fast, accurate, and robust ambiguity resolution but also an isometric array response.

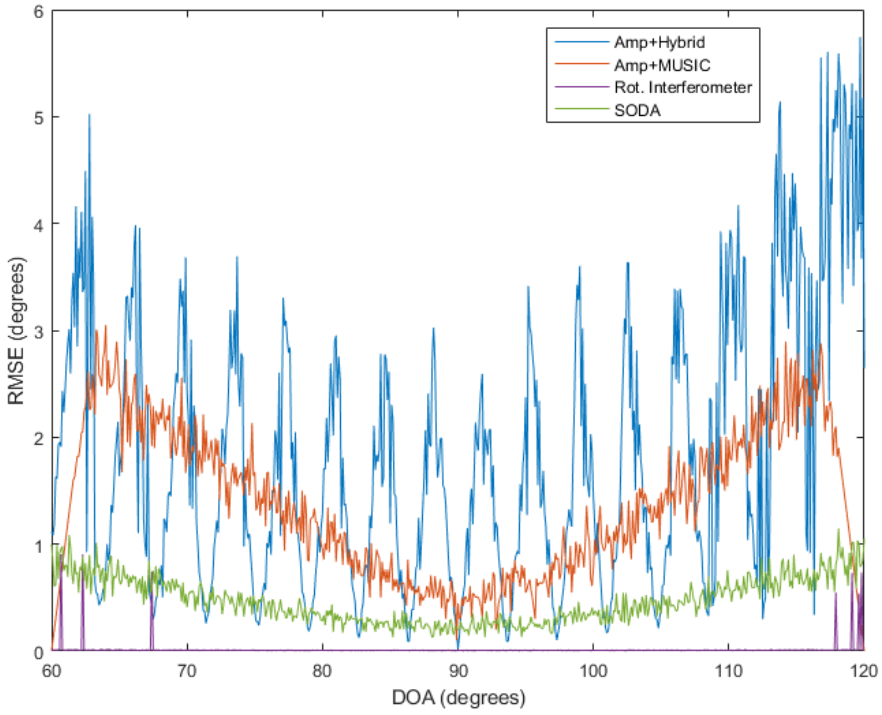

Figure 2.21. Comparison of Ambiguity Resolution Algorithms

.

CHAPTER 3

AMBIGUITY RESOLUTION WITH SODA ARRAY

In this chapter, a novel planar SODA array design is introduced, differing from the conventional linear SODA array approaches found in the literature. First, a planar SODA array is designed to meet specific constraints. The new approach is introduced in order to eliminate the Field-of-View (FOV) limitation of the designed planar array. Next, a rotary mechanism with an appropriate rotation frequency is applied to the array to enhance direction of arrival (DOA) estimation performance. Finally, all performance evaluations are compared against the Cramér-Rao Bound.

3.1 Planar SODA Array Design

The SODA array is typically examined in the literature with a linear configuration. However, in practical scenarios, linear arrangements are often impractical due to mounting constraints on ships, aircraft, or other vehicles. To address these issues, a planar SODA array structure can be employed.

Consider the SODA array with three elements given in Figure 3.1.Here, d_{12} denotes the distance between antenna 1 and antenna 2, d_{13} represents the distance between antenna 1 and antenna 3, and d_{23} is the distance between antenna 2 and antenna 3. The angle between baselines d_{13} and d_{12} is α, where $0 \leq \alpha \leq \pi/2$, $\lambda_{min}/2 \ll d_{12} \leq d_{13}$ and where λ_{min} the shortest wavelength is. The first order phase difference is introduced by

$$\psi_{21} = \frac{2\pi f(d_{\Delta})}{c}\cos(\varphi - \alpha) \tag{3.1}$$

$$\psi_{31} = \frac{2\pi f d_{\Delta}}{c}\cos(\varphi) \tag{3.2}$$

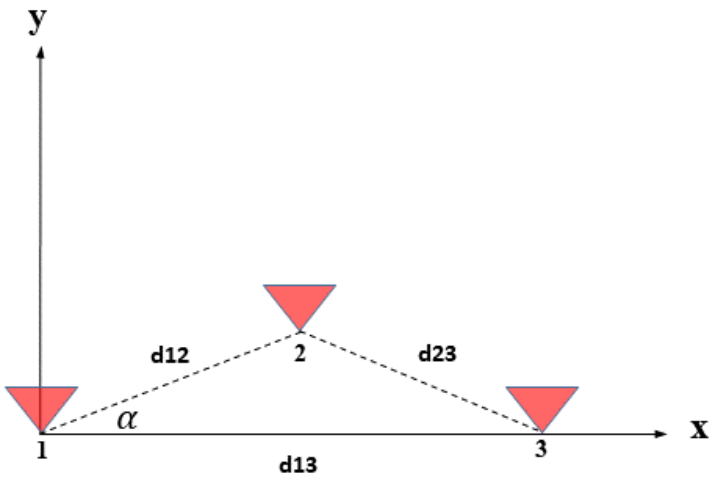

Figure 3.1. Planar SODA Array Geometry

The second order phase difference is given as

$$\psi_{\Delta} = \psi_{31} - 2\psi_{21} = \frac{2\pi f d_{\Delta}}{c}\cos(\varphi - \Theta) \tag{3.3}$$

where d_{Δ} is the second order distance and Θ is the rotation angle, and these are provided from cosine theorem as

$$d_{\Delta} = \sqrt{d^2{}_{13} - 4d^2{}_{12} - 4d_{12}d_{13}\cos\alpha} \tag{3.4}$$

$$\Theta = \arctan\left(\frac{-2d_{12}sin\alpha}{d_{13} - 2d_{12}cos\alpha}\right) \tag{3.5}$$

The second order phase difference term ψ_Δ is unambiguous when the following equation is satisfied.

$$0 < d_\Delta \leq \frac{\lambda_{min}}{2} \tag{3.6}$$

The corresponding the DOA estimation angle can be written as

$$\hat{\varphi} = \arccos\left(\frac{c\psi_\Delta}{2\pi f d_\Delta}\right) - \Theta \tag{3.7}$$

The distance d_{12} and the angle α can be described as [4]

$$d_{12} = \frac{d_{13}cos\alpha}{2} + \frac{1}{2}\sqrt{d^2{}_\Delta - d^2{}_{13}sin^2\alpha} \tag{3.8}$$

$$\alpha \leq arcsin\left(\frac{d_\Delta}{d_{13}}\right) \tag{3.9}$$

The second order phase difference ψ_Δ and second order distance d_Δ corresponds to virtual linear array with two elements rotated in angle Θ

The second-order phase difference ψ_Δ and the second-order distance d_Δ correspond to a virtual linear array consisting of two elements rotated by an angle Θ.

A planar SODA array with three elements functions similarly to a linear array, limiting its field of view (FOV) to 180°. Overcome this limitation, a novel planar SODA array design is proposed that allows for scanning the entire azimuth sector, thereby achieving a full 360° FOV.

3.2 Proposed Planar SODA Array Geometry

The proposed planar SODA array geometry given in Figure 3.2.

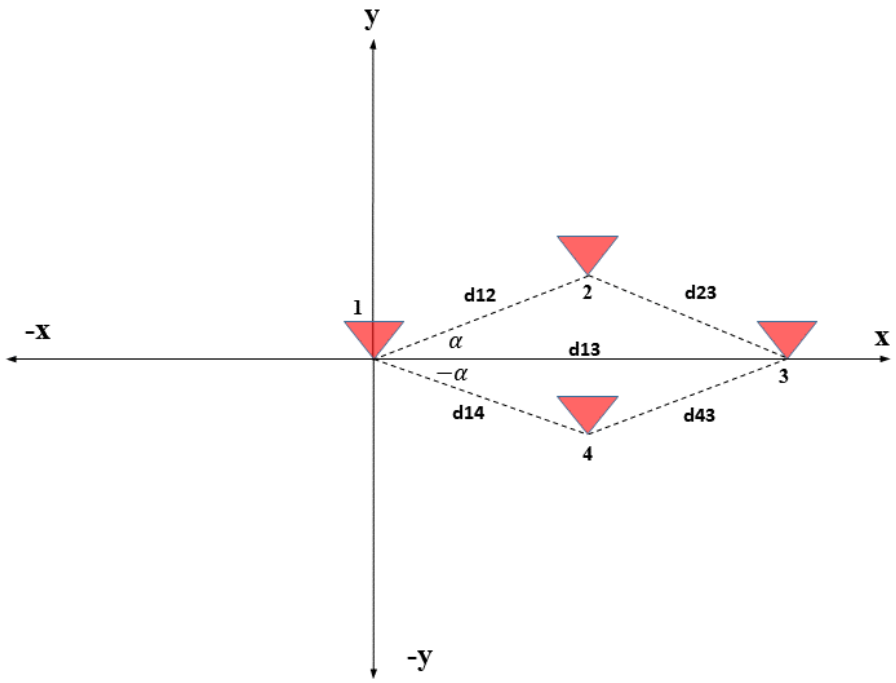

Figure 3.2. Proposed Planar SODA Array Geometry

The addition of a fourth antenna to this SODA array geometry allows for the design to achieve a 360° field of view (FOV) for direction of arrival (DOA) estimation. This

array structure enables accurate DOA estimation across the entire azimuth sector without ambiguity.

The second order phase differences can be written as follows;

$$\psi_{\Delta_1} = \psi_{31} - 2\psi_{21} = \frac{2\pi f d_{\Delta_1}}{c}\cos(\varphi - \Theta_1) = Q_1 \cos(\varphi - \Theta_1) \qquad (3.10)$$

$$\psi_{\Delta_2} = \psi_{31} - 2\psi_{41} = \frac{2\pi f d_{\Delta_2}}{c}\cos(\varphi - \Theta_2) = Q_2 \cos(\varphi - \Theta_2) \qquad (3.11)$$

where Q_1 and Q_2 are defined as $\frac{2\pi f d_{\Delta_1}}{c}$ and $\frac{2\pi f d_{\Delta_2}}{c}$ respectively. d_{Δ_1} and d_{Δ_2} can be found from Eqn. (3.4) Θ_1 and Θ_2 are described in Eqn. (3.5). By using cosine sum formula, Eqn. (3.10) and (3.11) can be rewritten as

$$Q_1 \cos(\varphi - \Theta_1) = Q_1(cos\varphi cos\Theta_1 + sin\varphi sin\Theta_1) \qquad (3.12)$$

$$Q_2 \cos(\varphi - \Theta_2) = Q_2(cos\varphi cos\Theta_2 + sin\varphi sin\Theta_2) \qquad (3.13)$$

Eqn. (3.10), Eqn. (3.11), Eqn. (3.12) and Eqn. (3.13) can be combined in $AX = B$ form as

$$\begin{bmatrix} cos\Theta_1 & sin\Theta_1 \\ cos\Theta_2 & sin\Theta_2 \end{bmatrix} \begin{bmatrix} cos\varphi \\ sin\ \varphi \end{bmatrix} = \begin{bmatrix} \psi_{\Delta_1}/Q_1 \\ \psi_{\Delta_2}/Q_2 \end{bmatrix} \qquad (3.14)$$

where, $A = \begin{bmatrix} cos\Theta_1 & sin\Theta_1 \\ cos\Theta_2 & sin\Theta_2 \end{bmatrix}$ and $X = \begin{bmatrix} cos\varphi \\ sin\ \varphi \end{bmatrix}$ and $B = \begin{bmatrix} \psi_{\Delta_1}/Q_1 \\ \psi_{\Delta_2}/Q_2 \end{bmatrix}$

In order to find, the pseudo-inverse of A can used as

$$X = (A^H A)^{-1} A^H B \tag{3.15}$$

where A^H is the hermitian of a matrix and $(A^H A)^{-1} A^H$ is the pseudo-inverse of A.

The DOA estimation angle can be found as [19]

$$\hat{\varphi} = \text{atan}\left(\frac{X(2)}{X(1)}\right) \tag{3.16}$$

where $X(1)$ and $X(2)$ are the first and second row of X respectively. This gives us Least Square Solution of DOA estimation angle φ [20].

3.3 Design Parameters of Proposed Planar SODA Array Geometry

Using Eqn. (3.4) , Eqn. (3.8) and (3.9) a planar SODA array geometry is designed as shown in Figure 3.2. This design allows for unambiguous DOA estimation over 360° FOV up to 18 GHz. Physical design parameters for the array are shown in Table 3.1.

Table 3.1 Planar SODA Array Design Parameters

Parameters	*Value*
d_{12}	0.07 meter
d_{13}	0.14 meter
d_{14}	0.07 meter
α	3°
Position of Antenna-1	(0,0)
Position of Antenna-3	(0.07,0) meter

At 18 GHz operating frequency, the derived parameters are listed in Table 3.2

Table 3.2 Planar SODA Array Derived Parameters

Parameters	*Value*
d_{Δ_1}	0.0073 meter
d_{Δ_2}	0.0073 meter
Θ_1	-88.5°
Θ_2	88.5°

Notice that for 18 GHz, $\lambda/2 = 0.0084$ and $d_{\Delta_{1,2}} < \lambda/2$. Hence ambiguity is solved for full azimuth scan of 360°. Figure 3.3 shows the two virtual SODA linear array which is equivalent to designed array shown in Figure 3.2 with the design parameters listed in Table 3.1 and Table 3.2.

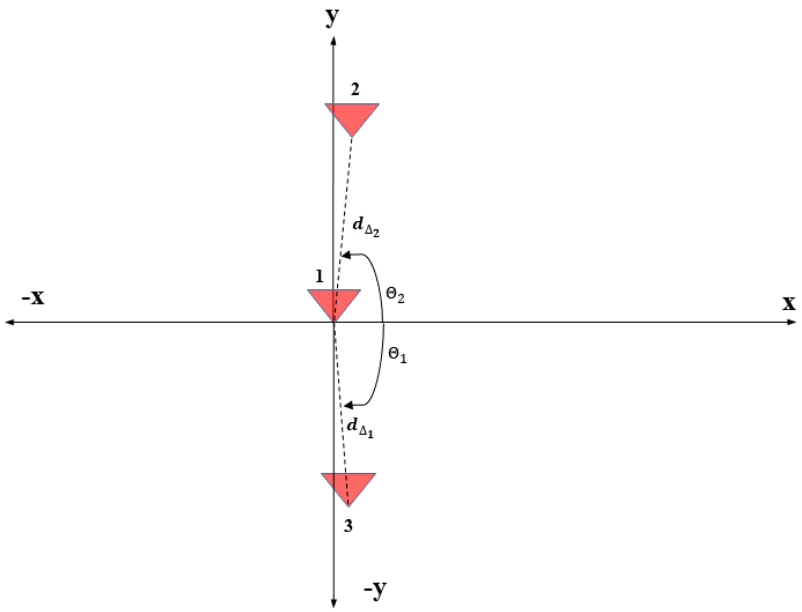

Figure 3.3. Equivalent Virtual SODA Array

3.4 Cramer-Rao Bound

Cramer-Rao bound (CRB) gives a lower bound of unbiased parameter estimation. An array comprising sensors that receives the signal emitted by far-field one narrowband source with direction parameters denoted by $\{\varphi_1\}$. Some assumptions are made in this section. The noise is a white Gaussian distributed noise, the source and signal are uncorrelated and there is only one target and only an azimuth scan is performed. The covariance matrix can be calculated as follows [21]

$$\boldsymbol{R} = \boldsymbol{APA}^* + \sigma \boldsymbol{I} \tag{3.17}$$

where $\boldsymbol{P}$ is the signal covariance matrix, σ is noise variance and $\boldsymbol{A}$ is the steering vector defined as

$$\boldsymbol{A} = [\boldsymbol{a}(\varphi_1)] \tag{3.18}$$

Due to the fact that we have only one source and perform only azimuth scan, we have an unknown parameter as

$$\alpha = \varphi \tag{3.19}$$

The Fisher information matrix (FIM) can be written as

$$FIM = NTr\left(\frac{d\boldsymbol{R}}{d\alpha}\boldsymbol{R}^{-1}\frac{d\boldsymbol{R}}{d\alpha}\boldsymbol{R}^{-1}\right) \tag{3.20}$$

$$FIM = F_{\varphi\varphi} \tag{3.21}$$

where N is the number of data snapshots, $Tr(.)$ is the trace operation and $F_{\varphi\varphi}$ is the azimuth estimator. The CRB of the angle parameter is defined as

$$CRB = FIM^{-1} \tag{3.22}$$

$$CRB(\varphi) = \frac{\sigma}{2N}\{Re(\boldsymbol{D}^{*}\boldsymbol{\Pi}_{\boldsymbol{A}}^{\perp}\boldsymbol{D}) \odot (\boldsymbol{P}\boldsymbol{A}^{*}\boldsymbol{R}^{-1}\boldsymbol{A}\boldsymbol{P})^{T}\}^{-1} \tag{3.23}$$

where $= \left(\frac{d\boldsymbol{a}(\varphi_1)}{d\varphi_1}\right)$, $\boldsymbol{\Pi_A^{\perp}} = \boldsymbol{I} - \boldsymbol{A}(\boldsymbol{A}^*\boldsymbol{A})^{-\mathbf{1}}\boldsymbol{A}^*$, $\odot$ is the Hadamard–Schur product, $(.)^*$is the conjugate transpose operator and $(.)^T$is the transpose operator.

3.5 Simulation Results of Proposed Planar SODA Array Geometry

The design parameters are given in Table 3.1 and Table 3.2. The simulation is performed according to parameters listed in Table 3.3

Table 3.3 Simulation Parameters

Parameter	*Value*
Frequency	18 GHz
SNR	40 dB,30 dB,20 dB,10 dB
Sampling Frequency	125 MHz
Number of Trials	100
Number of Snapshots	125

The performance results are given in Figure 3.4, Figure 3.5 and Figure 3.6

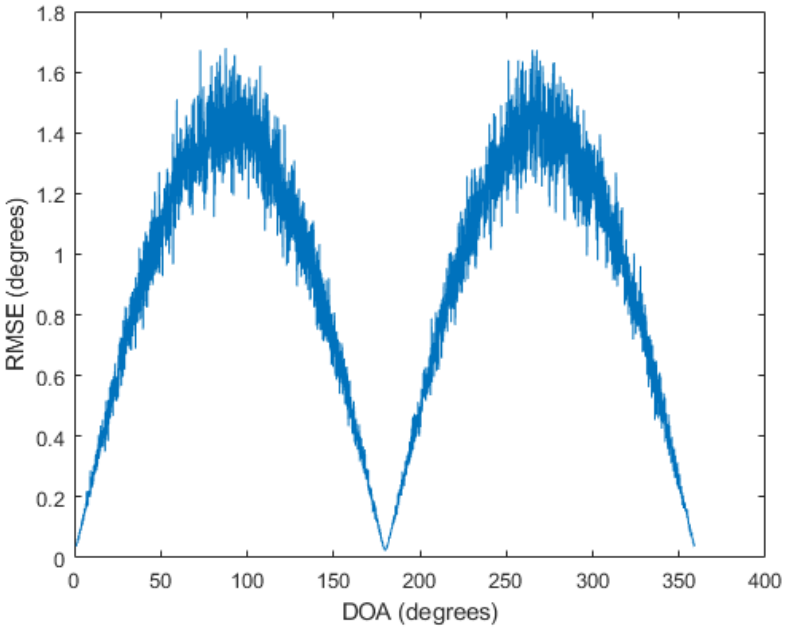

Figure 3.4. RMSE vs DOA, SNR =40 dB

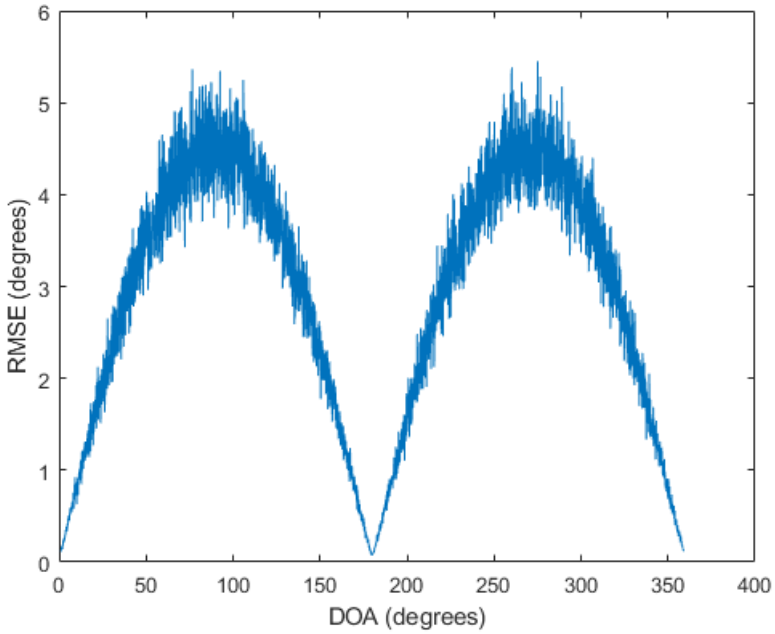

Figure 3.5. RMSE vs DOA, SNR =30 dB

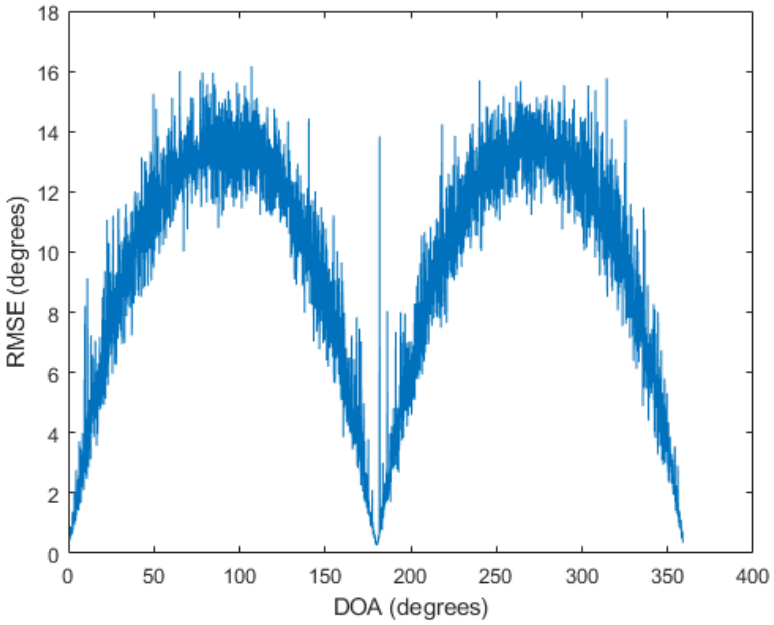

Figure 3.6. RMSE vs DOA, SNR =20 dB

In Figure 3.7, the performance of planar SODA array is compared with the CRB at an angle $\varphi = 60^{\circ}$.

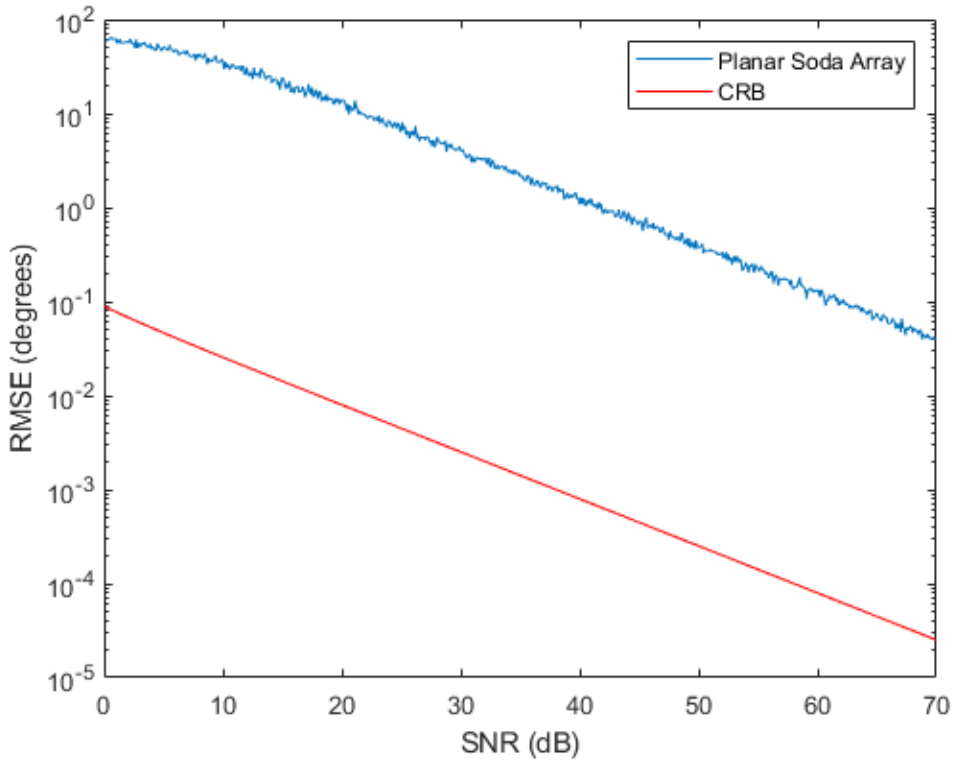

Figure 3.7. Planar Soda Array Performance, $\varphi = 60^{\circ}$

Figure 3.4, Figure 3.5, Figure 3.6 and Figure 3.7 show that the performance of the array is compromised in certain directions because of the linear structure of the virtual equivalent array. Additionally, due to the virtual small aperture $d_{\Delta_{1,2}} < \lambda/2$ achieving good performance requires a high SNR. To address these issues and achieve better, more robust performance, it is proposed to rotate the array to provide 360 degrees of coverage.

3.6 Proposed Rotating Planar SODA Array

The rotating SODA planar structure is shown in Figure 3.8. The source signal is observed by rotation SODA planar array with four antenna elements, 1, 2, 3 and 4 with initial (original) position is named as $1_{p_{initial}}$, $2_{p_{initial}}$, $3_{p_{initial}}$ and $4_{p_{initial}}$ respectively as discussed previously. Assume that the base-line 1-3 is rotating at a costant velocity by anticlockwise direction around Z-axis in XY plane. The angular rotation frequency is $\omega_r = 2\pi f_r$ where f_r is the rotation frequency and the rotation speed is $v_r = 2\pi f_r$. T is the rotation period. After Δt time all antenna elements are rotating from their own p_k location to p_{k+1} location. For example, after $\Delta\tau$ time, the array formation rotate from Figure 3.8 to Figure 3.9 or from Figure 3.10 to Figure 3.11. M is the number of data sampling points per rotation.

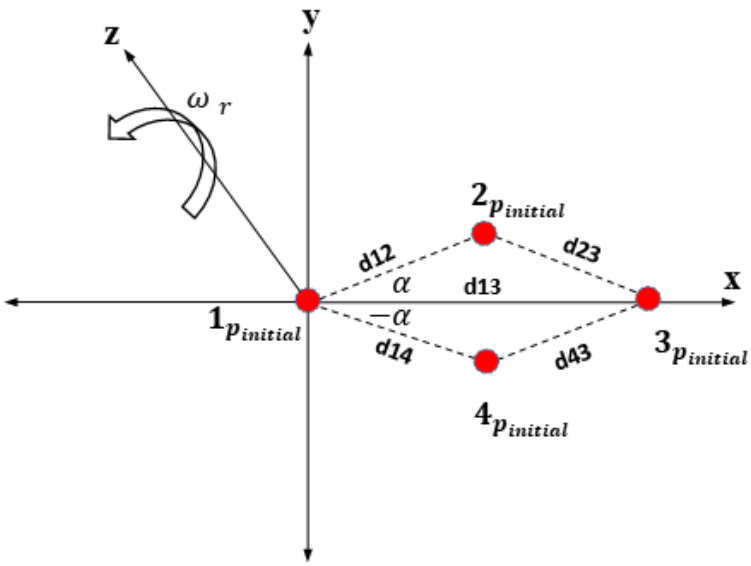

Figure 3.8. Rotating SODA Planar Array

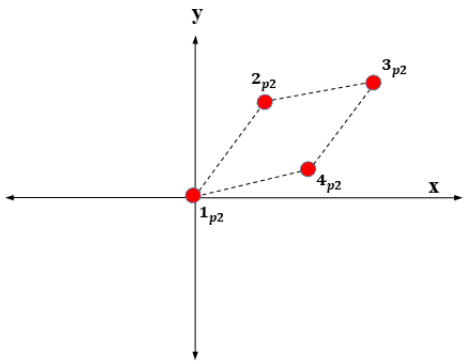

Figure 3.9. Rotating SODA Planar Array at p_2

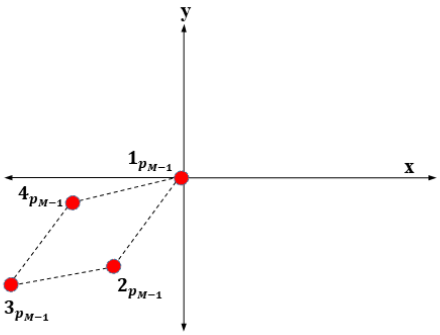

Figure 3.10. Rotating SODA Planar Array at p_{M-1}

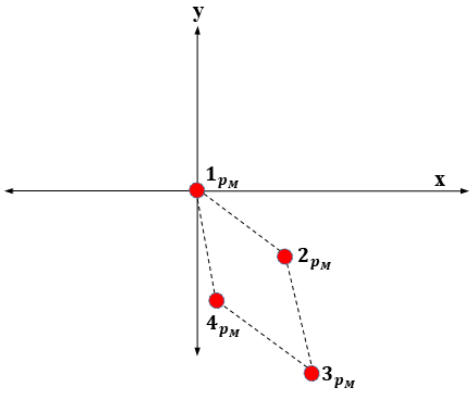

Figure 3.11. Rotating SODA Planar Array at p_M

To develop the proposed algorithm, we first need to clarify a few assumptions.

- Base-line 1-3 is rotating at a constant velocity.
- Select $4M$ elements at uniform time intervals to form a virtual SODA planar array within a time period of T.
- The source signal remains unchanged during the measurement period.

The signal model can be written as;

$$\boldsymbol{X}(t) = \boldsymbol{A}s(t) + N(t) \tag{3.24}$$

where $\boldsymbol{X}(t)$ is $4MxL$ array output vector, $\boldsymbol{A}$ is $4Mx1$ array steering vector and $s(t)$ is $1xL$ signal vector, $N(t)$ is $4Mx1$ noise vector and L is the number of snapshots.

The steering vector $\boldsymbol{A}$ can be expressed as

$$\boldsymbol{A}(\varphi) = [\boldsymbol{a_1}(\varphi), \boldsymbol{a_2}(\varphi), \dots, \boldsymbol{a_M}(\varphi)]^T \tag{3.25}$$

$$\boldsymbol{a_m}(\varphi) = [\boldsymbol{a_{1m}}(\varphi), \boldsymbol{a_{2m}}(\varphi), \boldsymbol{a_{3m}}(\varphi), \boldsymbol{a_{4m}}(\varphi)] \tag{3.26}$$

where $m = 1,2 \cdots, M$

$$a_{im}(\varphi) = exp(-jr_i \frac{2\pi}{\lambda} \cos(\varphi - \alpha_i - \frac{\omega_r}{M}(m-1))) \tag{3.27}$$

where $i = 1,2,3,4,\ r_1 = 0,\ r_2 = d_{12},\ r_3 = d_{13},\ r_4 = d_{14}$ and $\alpha_1 = 0^\circ,\ \alpha_2 = 3^\circ, \alpha_3 = 0^\circ, \alpha_4 = -3^\circ$

Eqn. (3.24) can be described as

$$x_{im}(t_m) = a_{im}(\varphi)s(t_m) + N_{im}(t_m) \tag{3.28}$$

where at the t_m, all four antennas begin sampling the signal. Phase differences can be written as

$$\tau_{im}(\varphi) = \frac{r_i}{c}\cos(\varphi - \alpha_i - \frac{\omega_r}{M}(m-1))) \tag{3.29}$$

t_m, can be written as

$$t_m = t_1 + (m-1)\Delta\tau \tag{3.30}$$

where $t_1 = 0$, $m = 1,2,\ldots M$ and $\Delta\tau$ is the time delay is the two neighboring data sampling point. After implementing $(m-1)\Delta\tau$ in Eqn. (3.28), it can be written as

$$x_{im}(t_m) = \exp(-j\omega(\tau_{im} + (m-1)\Delta\tau))s(t_m) + N_{im}(t_m) \tag{3.31}$$

$$x_{im}(t_m) = \exp(-j\omega(m-1)\Delta\tau)a_{im}(\varphi)s(t_m) + N_{im}(t_m) \tag{3.32}$$

It is assumed that source signal remains static, the rotation of array will cause Doppler frequency shift. Doppler frequency can be defined as [22]

$$f_{id} = \frac{2\pi f_r r_i \sin(\varphi - \omega_r t) f}{c} \tag{3.33}$$

where f is the source frequency. Hence ω in Eqn. (3.31) and (3.32) is updated as

$$\omega_i = 2\pi(f + f_{id}) \tag{3.34}$$

Define $\phi_{t_{im}} = \exp(-j\omega_i(m-1)\Delta\tau)$ as the phase difference of i^{th} antenna element at time t_m relative to their initial position. The phase difference matrix for all antenna elements at t_m can be defined as

$$\boldsymbol{\phi_{t_m}} = diag[\phi_{t_{1m}}, \phi_{t_{2m}} \cdots, \phi_{t_{im}}] \tag{3.35}$$

For all data sampling positions $m = 1,2, \ldots M$. Total phase difference matrix for all rotation points, M, can be written as

$$\boldsymbol{\phi} = diag[\boldsymbol{\phi_{t_1}}, \boldsymbol{\phi_{t_2}} \cdots, \boldsymbol{\phi_{t_M}}] \tag{3.36}$$

Finally, the signal model in Eqn. (3.24) is modified as

$$\boldsymbol{X}(t) = \boldsymbol{\phi A} s(t) + N(t) \tag{3.37}$$

where $\boldsymbol{X}(t)$ is $4MxL$ array output matrix, $\boldsymbol{\phi}$ is $4Mx4M$ phase difference matrix, the $\boldsymbol{A}$ is $4Mx1$ array steering vector and $s(t)$ is $1xL$ signal vector, $N(t)$ is $4Mx1$ noise vector and L is the number of snapshots.

3.7 Array Rotation Frequency

As the array rotates, the received signal data is sampled, leading to a small phase difference between each pair of sampled data points. To ensure the stability of the sampled data, $\Delta\tau$ must satisfy the following condition

$$T > \Delta\tau \gg \frac{1}{f_s} \tag{3.38}$$

where f_s is the sampling frequency. The time, $\Delta\tau$, can be defined as

$$\Delta\tau = \frac{T}{M} = \frac{1}{Mf_r} \tag{3.39}$$

The number of snapshots is L, then using Eqn. (3.38), it can be written as;

$$\frac{1}{f_r} > \frac{1}{Mf_r} \gg \frac{L}{f_s} \tag{3.40}$$

$$\frac{1}{f_r} > \frac{1}{Mf_r} \gg \frac{L}{f_s} \tag{3.41}$$

$$f_r \ll \frac{f_s}{ML} \tag{3.42}$$

Given a system sampling frequency of 125 MHz, 360 sampling points, and 125 snapshots, Eqn. (3.42) yields $f_r = 2.78$ kHz. If the array rotation frequency is

significantly lower than 2.78 kHz, the stability of the sampled data will be guaranteed.

3.8 DOA Estimation Algorithm

Recall from Eqn.(3.14), generalized form of $AX = B$ for rotation is given as

$$\begin{bmatrix} cos\Theta_1 & sin\Theta_1 \\ cos\Theta_2 & sin\Theta_2 \\ \vdots & \\ cos\Theta_{1M} & sin\Theta_{1M} \\ cos\Theta_{2M} & sin\Theta_{2M} \end{bmatrix} \begin{bmatrix} cos\varphi \\ sin\ \varphi \end{bmatrix} = \begin{bmatrix} \psi_{\Delta_1}/Q_1 \\ \psi_{\Delta_2}/Q_2 \\ \vdots \\ \psi_{\Delta_{1M}}/Q_1 \\ \psi_{\Delta_{2M}}/Q_2 \end{bmatrix} \tag{3.43}$$

where, $A = \begin{bmatrix} cos\Theta_1 & sin\Theta_1 \\ cos\Theta_2 & sin\Theta_2 \\ \vdots & \\ cos\Theta_{1M} & sin\Theta_{1M} \\ cos\Theta_{2M} & sin\Theta_{2M} \end{bmatrix}$ is the $2Mx2$ matrix and $X = \begin{bmatrix} cos\varphi \\ sin\ \varphi \end{bmatrix}$ is the $2x1$

vector and $B = \begin{bmatrix} \psi_{\Delta_1}/Q_1 \\ \psi_{\Delta_2}/Q_2 \\ \vdots \\ \psi_{\Delta_{1M}}/Q_1 \\ \psi_{\Delta_{2M}}/Q_2 \end{bmatrix}$ is the $2Mx1$ vector.

For all M points data sampling positions, elements of A and B is calculated.

Then in similar manner as discussed before, in order to find, the pseudo-inverse of A can used as

$$X = (A^H A)^{-1} A^H B \tag{3.44}$$

where A^H is the hermitian of a matrix and $(A^H A)^{-1} A^H$ is the pseudo-inverse of A.

The DOA estimation angle can be found as

$$\widehat{\varphi} = \text{atan}\left(\frac{X(2)}{X(1)}\right) \tag{3.45}$$

where $X(1)$ and $X(2)$ are the first and second row of X respectively. This gives us Least Square Solution of DOA estimation angle φ.

3.9 Rotating Planar SODA Array Simulation Results

The design parameters are given in Table 3.1 and Table 3.2. The rotation frequency is assumed to be 20 Hz, which is physically reasonable and ensures the stability of the algorithm. Additionally, M data sampling points in a rotation are considered. CRB is calculated according to the signal model described in Section 3.6. The simulation is performed according to parameters listed in Table 3.4

Table 3.4 Rotating Array Simulation Parameters

Parameter	*Value*
Frequency	18 GHz
SNR	40 dB,30 dB,20 dB
Rotation Frequency	20 Hz
Sampling Frequency	125 MHz
Number of Trials	10
Number of Snapshots	125
Number of Sampling Points	4 and 12

Increasing SNR and the data sampling points M significantly enhances the performance of the SODA array, as illustrated in Figure 3.12, Figure 3.13, Figure 3.14 and Figure 3.15. Specifically, when M is 4 and 12, the angular spacing between sampling points is $\pi/2$, and $\pi/6$, respectively. Comparing the rotating SODA array to the planar SODA array, the rotating configuration demonstrates a notable improvement in performance. Additionally, the rotating SODA array achieves an isometric array response, further optimizing its accuracy and effectiveness.

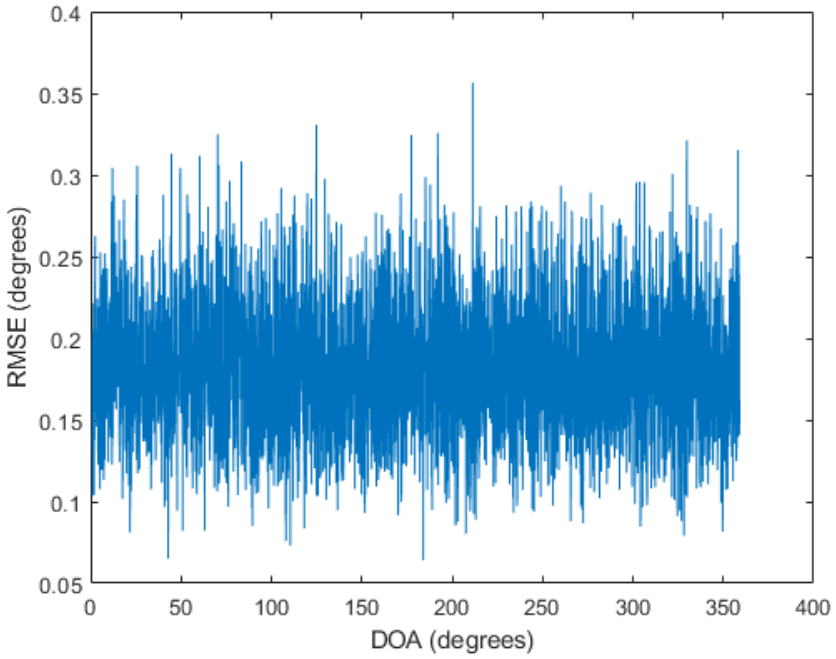

Figure 3.12. $M = 4, SNR = 20$ dB

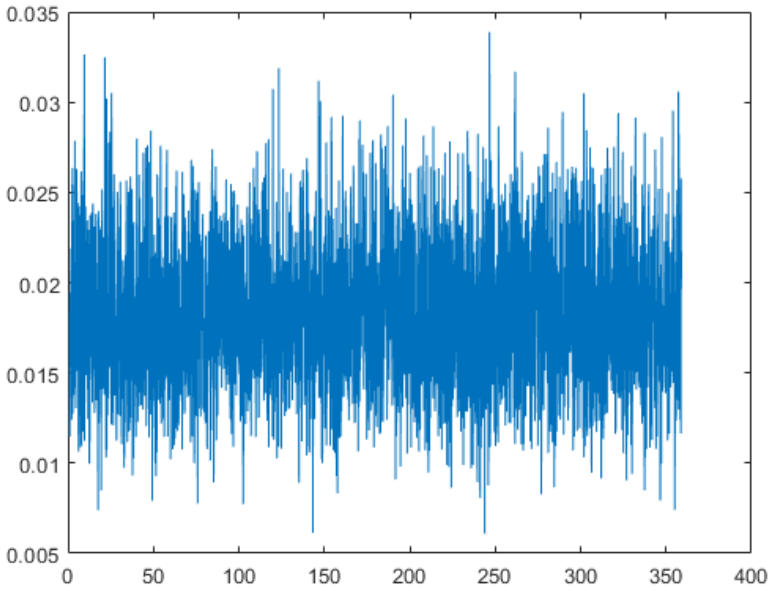

Figure 3.13. $M = 4, SNR = 40$ dB

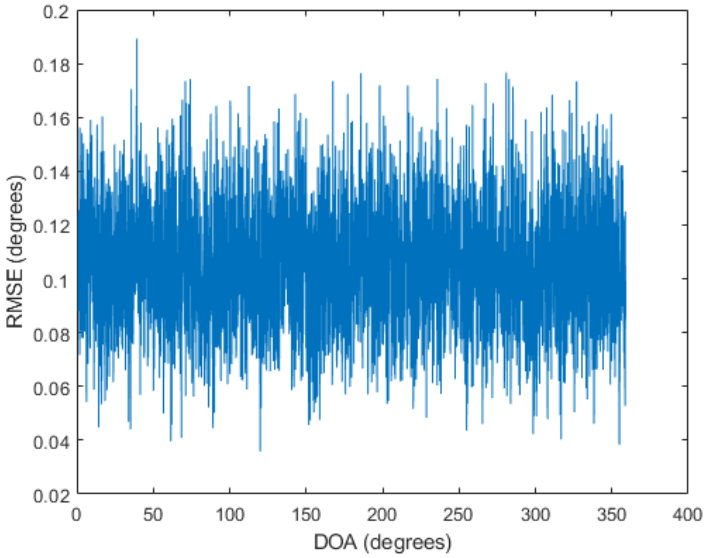

Figure 3.14. $M = 12, SNR = 20$ dB

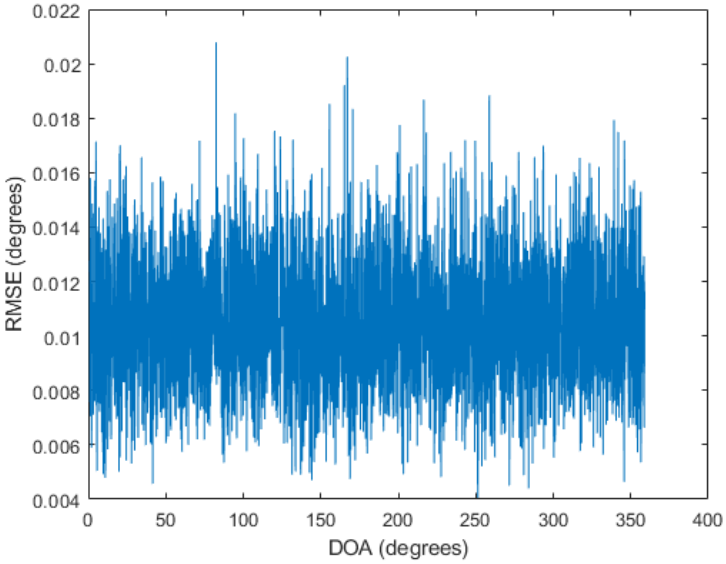

Figure 3.15. $M = 12, SNR = 40$ dB

Rotating SODA array performance respect to Planar SODA array and CRB is given in Figure 3.16, and Figure 3.17. The CRB curves, as the number of sampling points M increases, demonstrate that the performance of the rotating SODA array improves more significantly compared to the planar SODA array. Specifically, these curves reveal that the rotating SODA array achieves greater accuracy and lower estimation errors, showcasing its superior ability to resolve ambiguities and enhance overall performance.

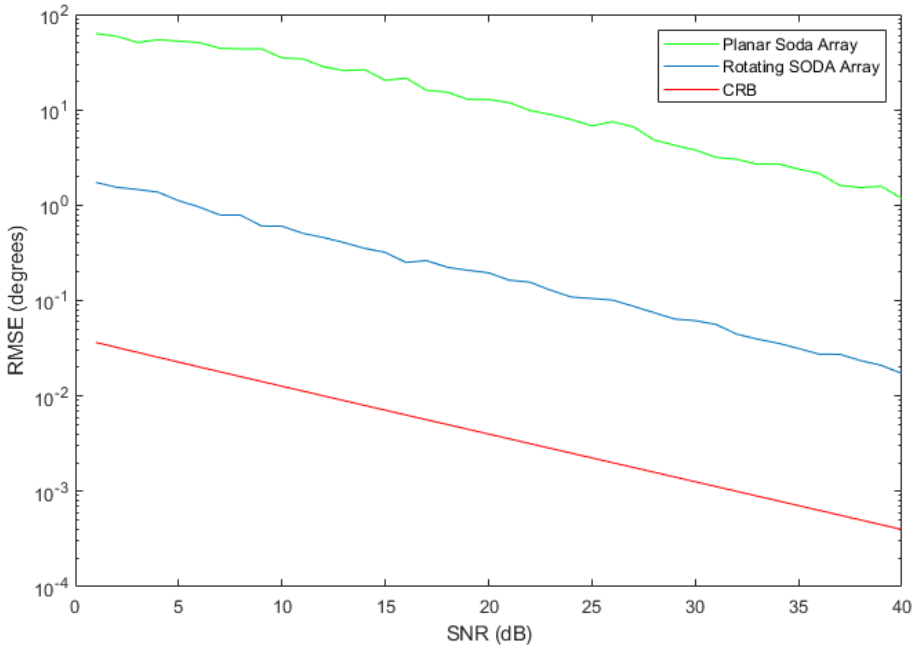

Figure 3.16. $M = 4$

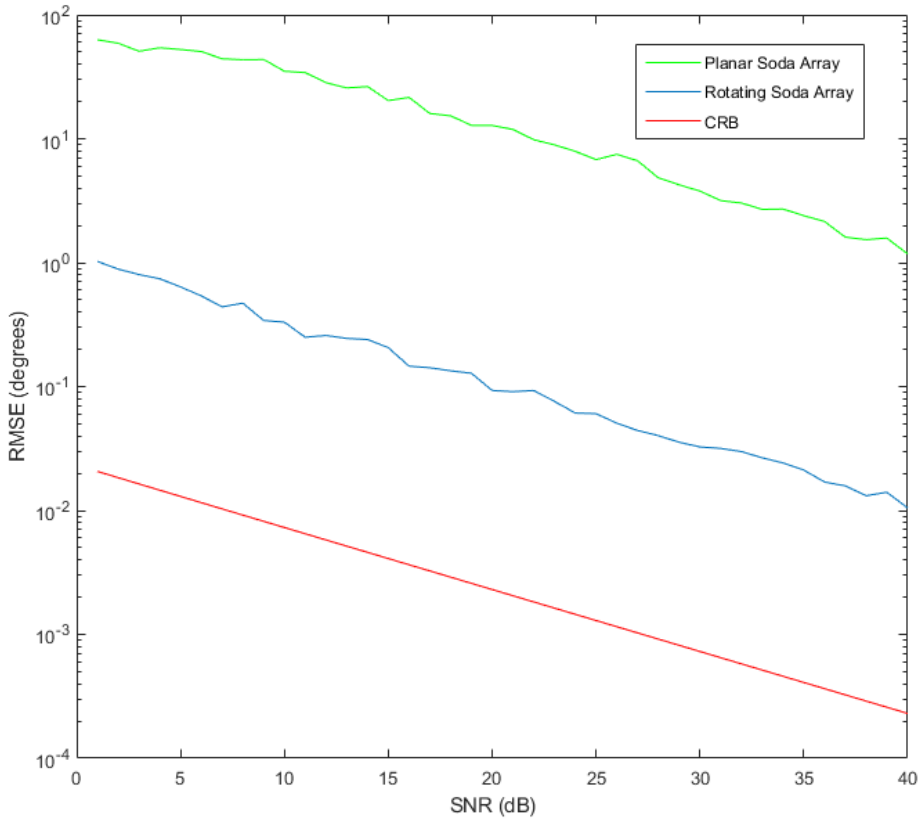

Figure 3.17. $M = 12$

3.10 The DOA Performance with Varying Rotation Frequencies

In Section 3.7 of this thesis, it is explained that the rotation frequency is set to a reasonable level to maintain signal coherence during data collection. In other words, since the sampling frequency is significantly higher than the rotation frequency, the array appears stationary during the data collection process. For instance, with a rotation frequency of 100 Hz and a total data sampling time of 1μsec at a sampling frequency 125 MHz, 125 snapshots are captured. The angular displacement in this case will be $2\pi * 100 * 10^{-6} = 6.283210^{-4}\, radian$. Therefore, the goal is to

examine the DOA performance of the rotating SODA array as the rotation frequency varies. The simulation is performed according to parameters listed in Table 3.5

Table 3.5 Rotating Array Simulation Parameters

Parameter	*Value*
Frequency	18 GHz
SNR	20 dB
Rotation Frequency, f_r	1-100 Hz
Frequency Increment Step	1 Hz
Sampling Frequency	125 MHz
Number of Trials	100
Number of Snapshots	125
Number of Sampling Points	4

Figure 3.18, illustrates how the DOA performance varies with changes in rotation frequency. It is observed that although any phase compensation is not applied, the DOA performance for all angles of the rotating SODA array is good at certain rotation frequencies. However, at other frequencies, the DOA performance deteriorates.

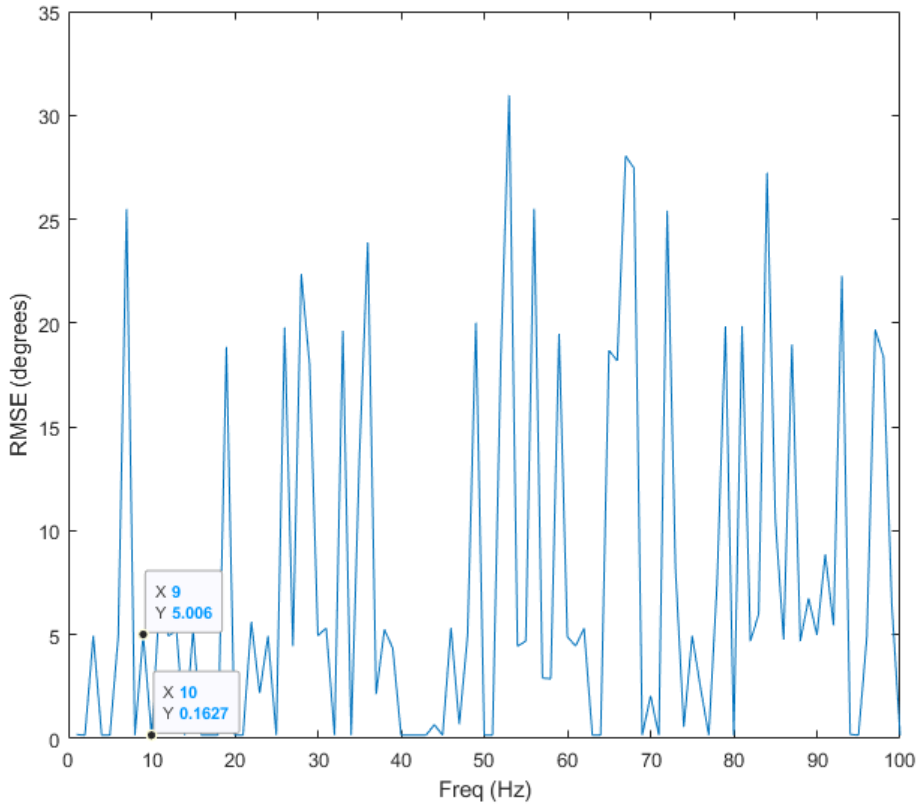

Figure 3.18. RMSE vs Rotating Frequency

For example, the rotation frequencies of 9 Hz and 10 Hz are examined. At 9 Hz, the performance of the rotating SODA array deteriorates, while at 10 Hz, the performance is good. The phase disturbance of the phase difference between Antenna-1 and Antenna-3 (ψ_{31}) is calculated and presented in the figures for 9 Hz and 10 Hz frequencies at four data sampling points. M is equal to four and the angular spacing between sampling points is $\pi/2$. The phase disturbance refers to the phase deviation that occurs when the array rotates, compared to when it remains stationary. This deviation arises due to the relative motion between the array elements and the signal sources, resulting in changes in the phase of the received signals. As the array rotates, the time delay and Doppler shift introduce phase changes that can affect the accuracy of DOA estimation if not properly compensated.

The phase disturbance of the phase difference between Antenna-1 and Antenna-3 (ψ_{31}) for 9 Hz is shown in Figure 3.19, Figure 3.20, Figure 3.21and Figure 3.22.

In Figure 3.19, it is observed that phase disturbance solely due to Doppler shift, which starts to occur as the rotation begins. In Figure 3.20, when the array rotation angle is 90°, phase disturbance caused by both time delay and Doppler shift is observed.

In Figure 3.21 and Figure 3.22 when the array rotation angle is 180° and 270°, respectively, we observe further phase disturbance caused by both time delay and Doppler shift. In fact, at this rotation frequency, the phase disturbance due to time delay is more significant than the disturbance from Doppler shift.

The phase disturbance of the phase difference between Antenna-1 and Antenna-3 (ψ_{31}) for 10 Hz is shown in Figure 3.23 Figure 3.24 Figure 3.25 and Figure 3.26. From these figures, it is observed that there is no additional disturbance from time delay for all rotation angles. The phase disturbance is primarily attributed to the Doppler frequency alone.

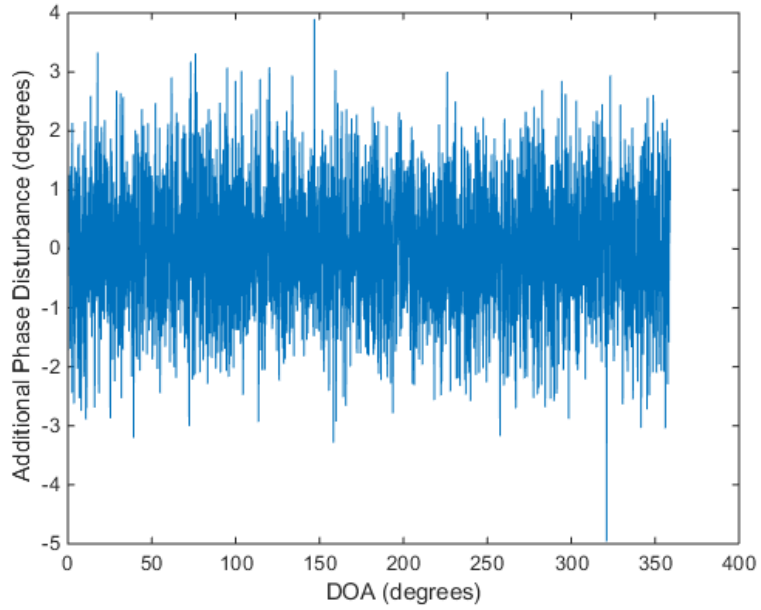

Figure 3.19. $f_r = 9\ Hz, m = 1,\ Array\ Rotation\ Angle = 0°$

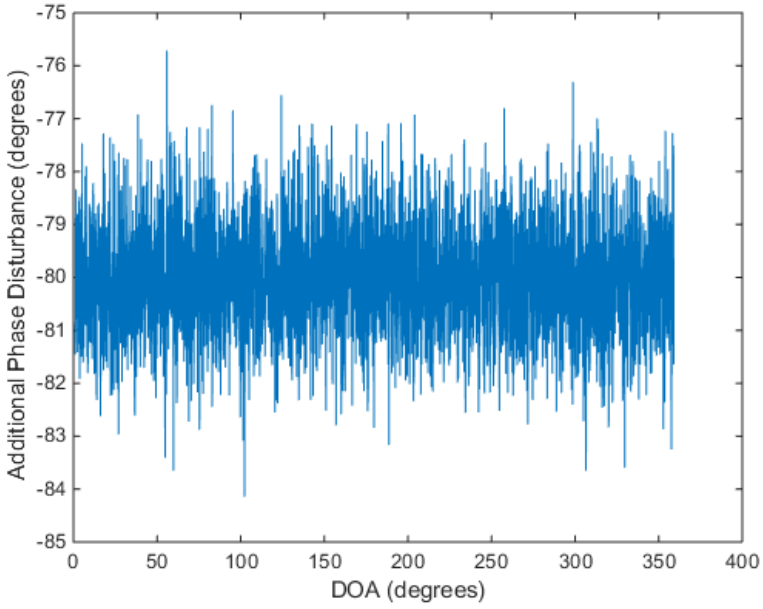

Figure 3.20. $f_r = 9\ Hz, m = 2, Array\ Rotation\ Angle = 90°$

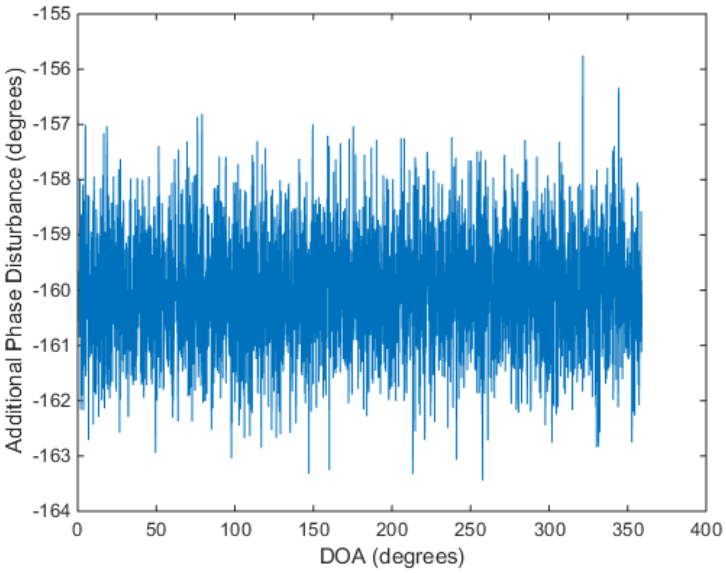

Figure 3.21. $f_r = 9\ Hz, m = 3$, $Array\ Rotation\ Angle = 180°$

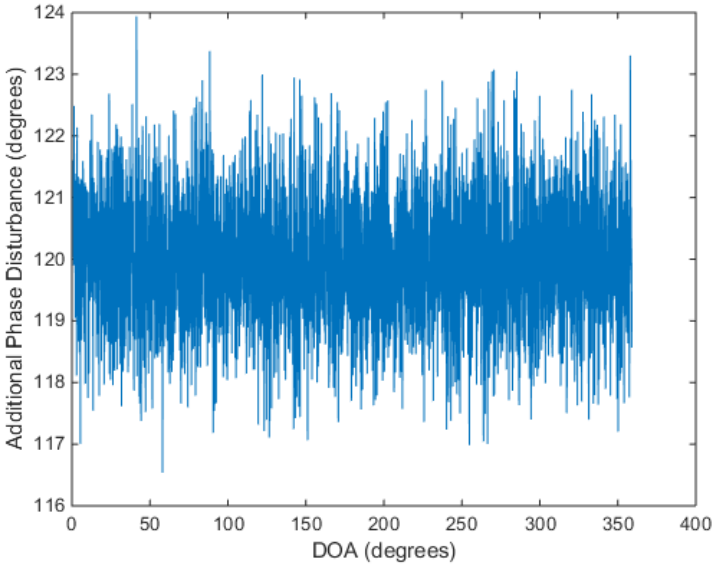

Figure 3.22. $f_r = 9\ Hz, m = 3, Array\ Rotation\ Angle = 270°$

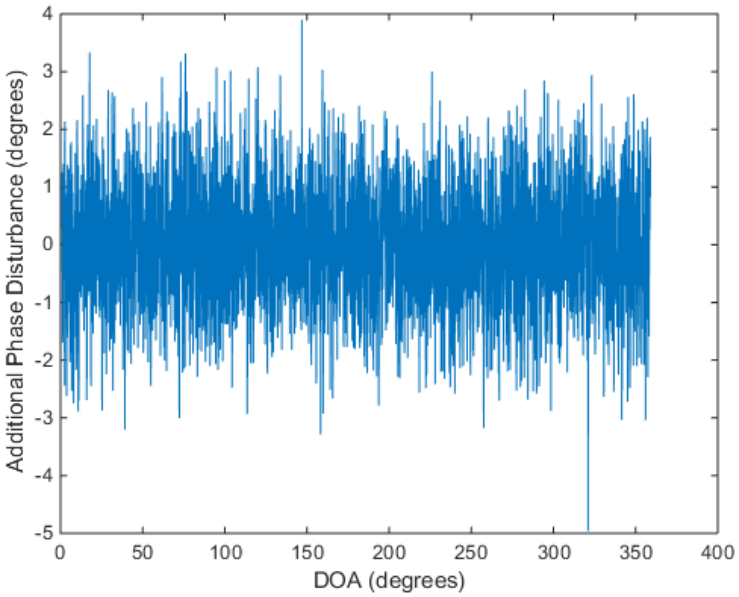

Figure 3.23. $f_r = 10\ Hz, m = 1, Array\ Rotation\ Angle = 0°$

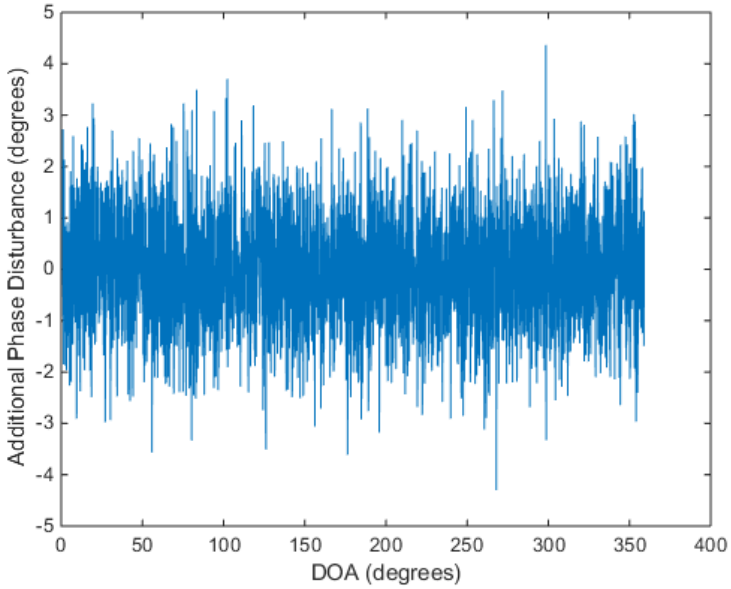

Figure 3.24. $f_r = 10\ Hz, m = 2, Array\ Rotation\ Angle = 90°$

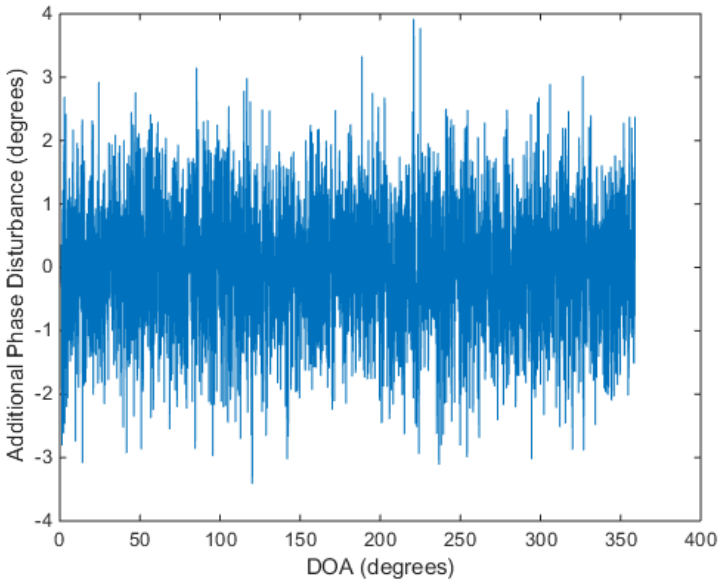

Figure 3.25. $f_r = 10\ Hz, m = 3, Array\ Rotation\ Angle = 180°$

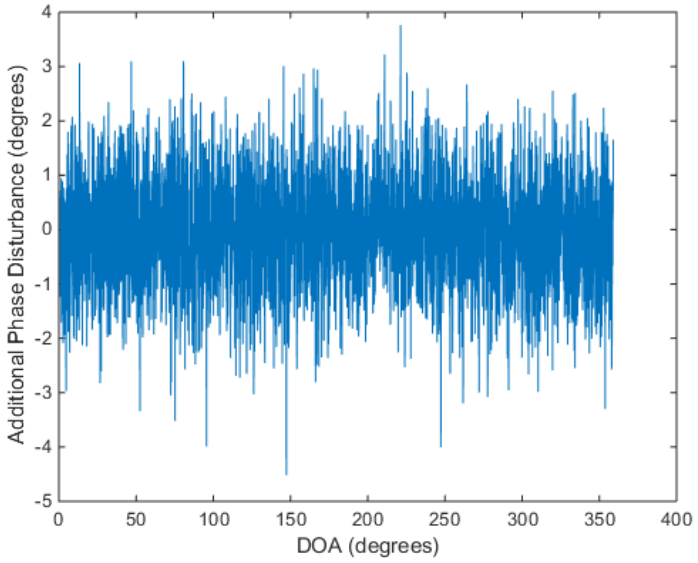

Figure 3.26. $f_r = 10\ Hz, m = 4, Array\ Rotation\ Angle = 270°$

Consider, $\phi_{d_{im}} = \exp(-j\omega(m-1)\Delta\tau)$ as the phase difference of i^{th} antenna element at time t_m relative to their initial position, sampling points $m = 1,2, \ldots M$ $\Delta\tau = \frac{1}{M*f_r}$ is the time delay is the two neighboring data sampling point, ω is the radial frequency of the source signal. If Eqn. (3.46) is satisfied, the phase disturbance $\phi_{d_{im}}$ is due to time delay could be eliminated.

$$mod(\omega(m-1)\Delta\tau, 2\pi) \approx 0 \tag{3.46}$$

When examining the phase disturbance, it arises from the time delay between data sampling points and the Doppler frequency due to the rotation frequency. At a reasonable rotation frequency, the phase disturbance caused by the Doppler frequency is negligible compared to the phase disturbance caused by the time delay. At 9 Hz, it is observed that the phase disturbance is influenced by both the time delay and the Doppler effect. In contrast, at 10 Hz, the phase disturbance is primarily due to the Doppler frequency alone. In other words, in the case of $f_r = 10$, Eqn. (3.46) is satisfied.

To achieve more stable and robust DOA performance for the SODA rotating array across different operating frequencies, the phase disturbance caused by the time delay must first be compensated.

3.11 Phase Compensation Due to Time Delay

Time Delay Compensation procedure is explained in this section.

Define, $\phi_{dc_i} = \exp(j\omega(m-1)\Delta\tau)$ as the time-delay compensation element of i^{th} antenna element at time t_m relative to their initial position where sampling points

$m = 1,2, \ldots M$, $\Delta\tau = \frac{1}{M * f_r}$ is the time delay is the two neighboring data sampling point, ω is the radial frequency of the source signal, f_r is the rotation frequency.

The time-delay compensation matrix for all antenna elements at t_m can be defined as

$$\boldsymbol{\phi_{dc_m}} = diag[\phi_{dc_{1m}}, \phi_{dc_{2m}} \cdots, \phi_{dc_{im}}] \tag{3.47}$$

For all data sampling positions $m = 1,2, \ldots M$. Total time-delay compensation matrix for all rotation points, M, can be written as

$$\boldsymbol{\phi_{dc}} = diag[\boldsymbol{\phi_{dc_1}}, \boldsymbol{\phi_{dc_2}} \cdots, \boldsymbol{\phi_{dc_M}}] \tag{3.48}$$

Finally, the signal model in Eqn. (3.37) is modified to incorporate the time-delay compensation, resulting in the following time-delay compensated signal model;

$$\boldsymbol{X_{dc}}(t) = \boldsymbol{\phi_{dc}}\boldsymbol{X}(t) \tag{3.49}$$

where $\boldsymbol{X}(t)$ is $4MxL$ array output matrix, $\boldsymbol{\phi_{dc}}$ is $4Mx4M$ time-delay compensation matrix, $\boldsymbol{X_{dc}}(t)$ is $4MxL$ time-delay compensated array output matrix and L is the number of snapshots.

After the time-delay compensation process, the simulation is performed again using the parameters listed in Table 3.5. The results are shown in Figure 3.27. After the time-delay compensation process, the rotating SODA array performs well across all relevant rotation frequencies. Additionally, specifically when $f_r = 9\ Hz$, following

the time-delay compensation process, the rotating SODA array performs effectively shown in the Figure 3.28.

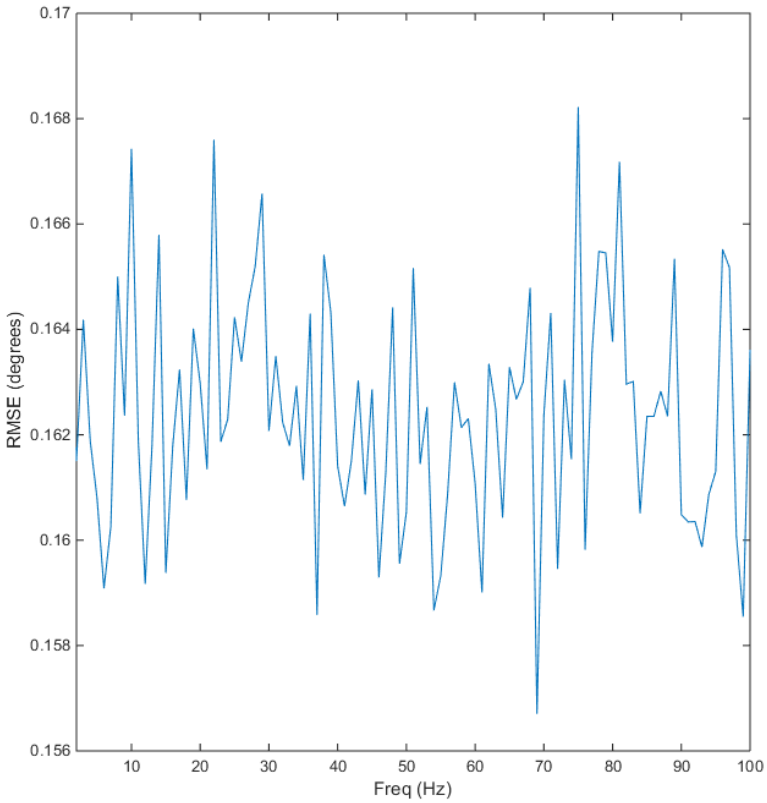

Figure 3.27. RMSE vs Rotating Frequency (After Time-Delay Compensated)

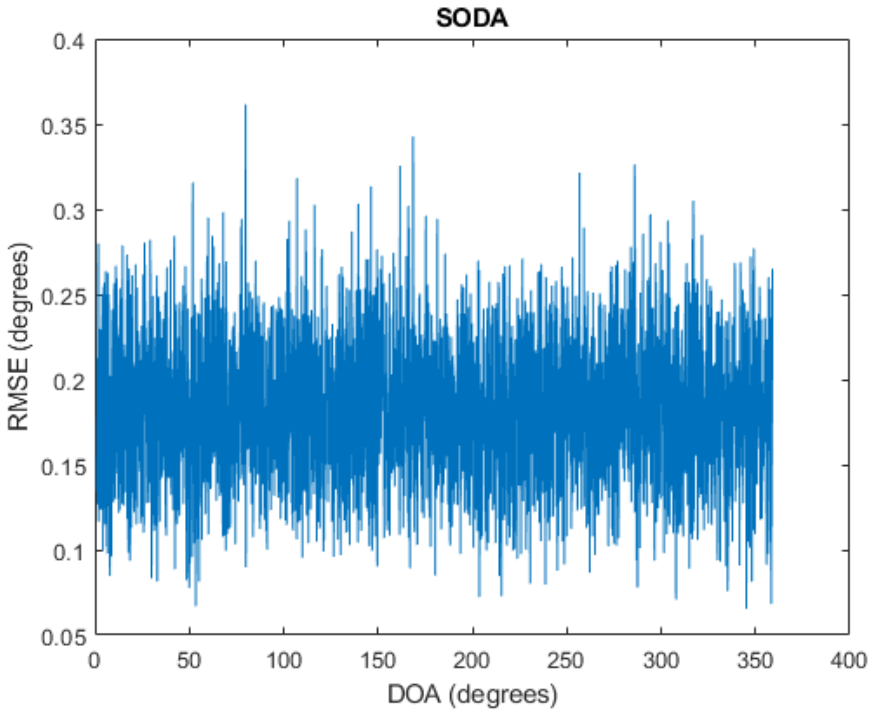

Figure 3.28. $f_r = 9\ Hz$ (After Time-Delay Compensated)

3.12 Rotating Planar SODA Array and MUSIC Hybrid Technique

The MUSIC algorithm is a super-resolution technique that provides high accuracy and resolution in DOA estimation. However, it still faces issues with ambiguity, which can be resolved by using the SODA method. Furthermore, when the MUSIC algorithm is combined with the rotating SODA array, the array manifold vector is virtually increased, improving the system's resolution and accuracy in DOA estimation, which enables optimal DOA performance.

The details about MUSIC and rotating SODA algorithms are given in Section 2.4.and Section 3.8 respectively. The received signal is given in Eqn. (3.49).

Rotating SODA and MUSIC Hybrid algorithm flows as follows;

i. Perform Rotating SODA algorithm and obtain the unambiguous DOA angle $\widehat{\boldsymbol{\varphi}}_{\mathbf{SODA}}$

ii. Perform MUSIC algorithm and angle-search in the MUSIC pseudo spectrum within $\hat{\varphi}_{\mathrm{SODA}} - 3 * \hat{\varphi}_{\mathrm{SODA}_{RMS}} \leq \vartheta_{\mathrm{MUSIC}_{search}} \leq \hat{\varphi}_{\mathrm{SODA}} + 3 * \hat{\varphi}_{\mathrm{SODA}_{RMS}}$

iii. Find the DOA angle $\widehat{\boldsymbol{\varphi}}_{\boldsymbol{final}}$ of the corresponding peak in the MUSIC pseudo spectrum within the given interval

3.13 Rotating Planar SODA Array and MUSIC Hybrid Technique Results

The simulation is performed according to parameters listed in Table 3.6.

Table 3.6 Rotating Array Simulation Parameters

Parameter	*Value*
Frequency	18 GHz
SNR	20 dB
Rotation Frequency	20 Hz
Sampling Frequency	125 MHz
Number of Trials	100
Number of Snapshots	125
Number of Sampling Points	4

The DOA performance of SODA and MUSIC Hybrid Technique is shown in Figure 3.29. It can be seen that the MUSIC algorithm significantly enhances the rotating SODA array with respect to Figure 3.12. It effectively behaves like an M-element circular virtual array, providing an isometric, ambiguity-free, and high-accuracy DOA response.

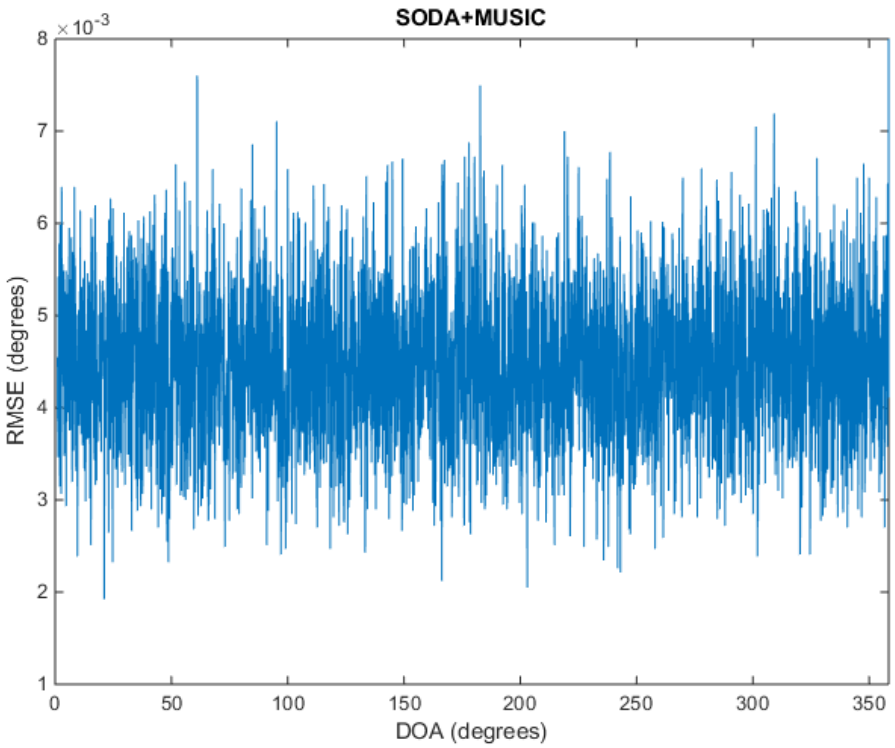

Figure 3.29. $M = 4, SNR = 20$ dB

Rotating SODA array and SODA+MUSIC Hybrid techniques performance respect to CRB are given in Figure 3.30. It can be seen from the figure that while MUSIC enhances the performance of the rotating SODA array, the MUSIC+SODA performance does not converge to the Cramer-Rao Bound due to phase imbalance caused by the Doppler effect during the M data sampling points. In other words, MUSIC algorithm is significantly affected by the Doppler effect due to rotation. Therefore, a phase compensation approach to address the Doppler effects must be utilized [23].

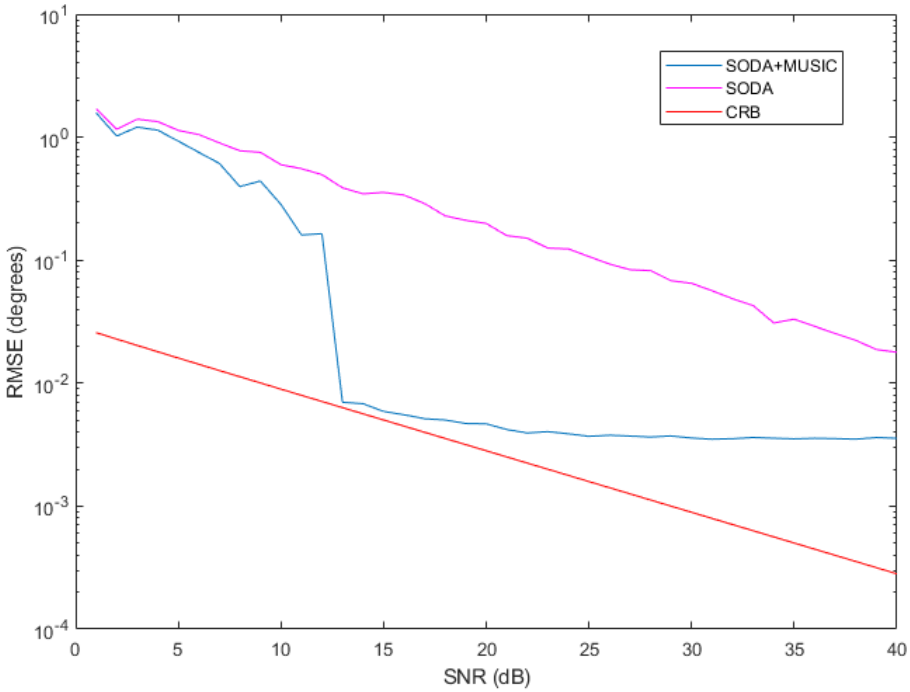

Figure 3.30. $M = 4$

3.14 Phase Compensation Due to Doppler Effects

Due to the proposed planar SODA array geometry and its rotation mechanism, the Doppler frequency for the three rotating antennas is measured relative to the first antenna, as the first antenna remains stationary and experiences zero Doppler shift. This can be used to estimate the Doppler frequencies for the three rotating antennas.

Define $\phi_{fc_{im}}(t) = \exp(-j\omega_{d_{im}}(t-(m-1))\Delta\tau)$ as the doppler phase compensation element of i^{th} antenna element at time t_m relative to their initial position where sampling points $m = 1,2,\dots M$, $\omega_{d_{im}}$is the radial doppler frequency of i^{th} antenna element at time t_m , $\Delta\tau = \frac{1}{M*f_r}$ is the time delay is the two neighboring data sampling, L is the number of snapshots.

Phase Compensation Procedure flows as follow;

i. Obtain $s_{im}[n]$ signal at t_m. Where $s_{im}[n]$ is the sampled signal of i^{th} antenna element at time t_m relative to their initial position where sampling points $m = 1,2,\dots M, i = 1,2,3,4,\ t_1 = 0,\ t_m = t_1 + (m-1)\Delta\tau$, $\Delta\tau = \frac{1}{M*f_r}$ is the time delay is the two neighboring data sampling

ii. Estimate $\omega_{d_{im}}$ at t_m [24]

$$\omega_{d_{im}} = 2\pi\left(\frac{\underset{k_{im}}{\text{argmax}}|DFT(s_{im}[n])| - \underset{k_{1m}}{\text{argmax}}|DFT(s_{im}[n])|}{L}\right)f_s \qquad (3.50)$$

Where $\omega_{d_{im}}$is the radial doppler frequency of i^{th} antenna element at time t_m, DFT is the Discrete Fourier Transform, f_s is the sampling frequency, L is the number of snapshots, k_{im} corresponds to the largest magnitude in Hertz in the DFT of $s_{im}[n]$.

iii. Obtain $\phi_{fc_{im}}(n) = \exp(-j\omega_{d_{im}}(n-(m-1))\Delta\tau)$ as the $1xL$ doppler compensation array of i^{th} antenna element at time t_m

iv. Obtain $\boldsymbol{\phi_{fc_m}}$ the $4xL$ doppler compensation matrix for all antennas at time t_m

$$\boldsymbol{\phi_{fc_m}} = [\boldsymbol{\phi_{fc_{1m}}}^T, \boldsymbol{\phi_{fc_{2m}}}^T \cdots, \boldsymbol{\phi_{fc_{im}}}^T]^T \qquad (3.51)$$

v. Obtain $\boldsymbol{\phi_{fc}}$ the $4MxL$ total doppler compensation matrix for all antennas for all t_m

$$\boldsymbol{\phi_{fc}} = [\boldsymbol{\phi_{dc_1}}^{\boldsymbol{T}}, \boldsymbol{\phi_{dc_2}}^{\boldsymbol{T}}, \cdots, \boldsymbol{\phi_{dc_M}}^{\boldsymbol{T}}]^T \tag{3.52}$$

vi. Obtain the signal model in Eqn.(3.49) which is updated to include doppler compensation, resulting in the following $4MxL$ time-delay and doppler-compensated signal model, $\boldsymbol{X_{fd_c}}$

$$\boldsymbol{X_{fd_c}}(t) = \boldsymbol{\phi_{fc}} \odot \boldsymbol{X_{dc}}(t) \tag{3.53}$$

where $\odot$ is the Hadamard–Schur product, $(.)^T$ is the transpose operator, $\boldsymbol{X_{fd_c}}(t)$ is $4MxL$ time-delay and doppler compensated array output matrix, $\boldsymbol{\phi_{fc}}$ is $4MxL$ total doppler compensation matrix, $\boldsymbol{X_{dc}}(t)$ is $4MxL$ only time-delay compensated array output matrix and L is the number of snapshots.

3.15 Revisited Rotating Planar SODA Array and MUSIC Hybrid Technique Results

In this section $\boldsymbol{X_{fd_c}}(t)$, the time-delay and Doppler-compensated array output matrix given in Eqn.(3.53), is used to analyze the DOA performance of the rotating SODA array. The simulation is performed according to parameters listed in Table 3.6.

The DOA performance of the SODA-MUSIC hybrid algorithm on time-delay and Doppler-compensated data are shown in Figure 3.31. The performance of the SODA-MUSIC hybrid algorithm is better than the case where only time-delay compensation is applied, as depicted in the Figure 3.29.

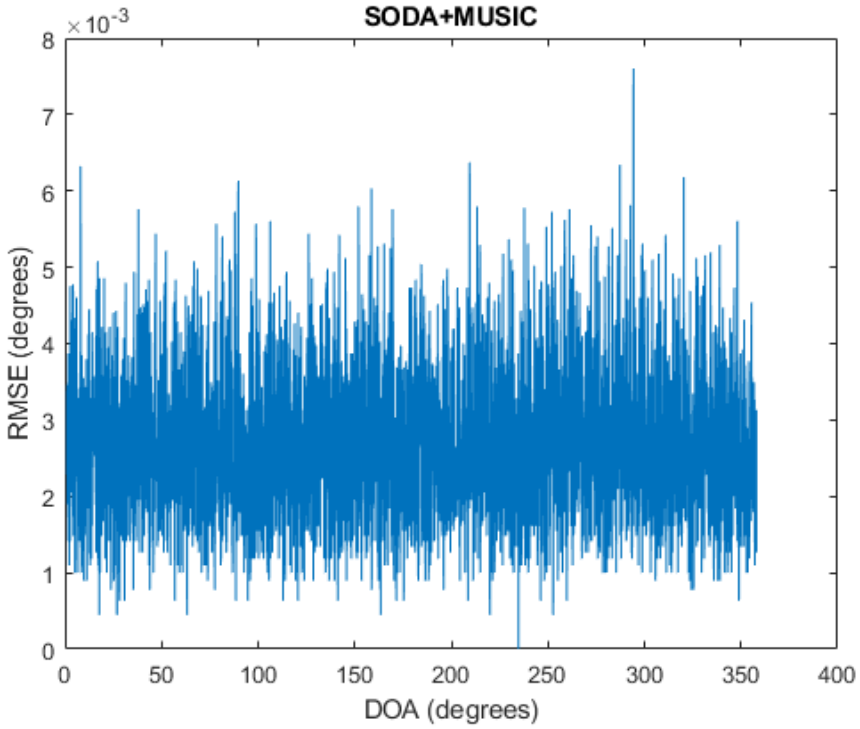

Figure 3.31. $M = 4, SNR = 20$ dB

The performance of the rotating SODA array and the SODA+MUSIC hybrid technique with respect to the Cramer-Rao Bound (CRB) is shown in Figure 3.32. After the Doppler compensation process, the rotating SODA and MUSIC Hybrid algorithm performs close-to-optimum DOA estimation, and the estimation error asymptotically approaches the Cramer-Rao Bound. Although the MUSIC algorithm shows improved performance after Doppler compensation, the performance of the rotating SODA algorithm does not change significantly which is also shown in Figure 3.33

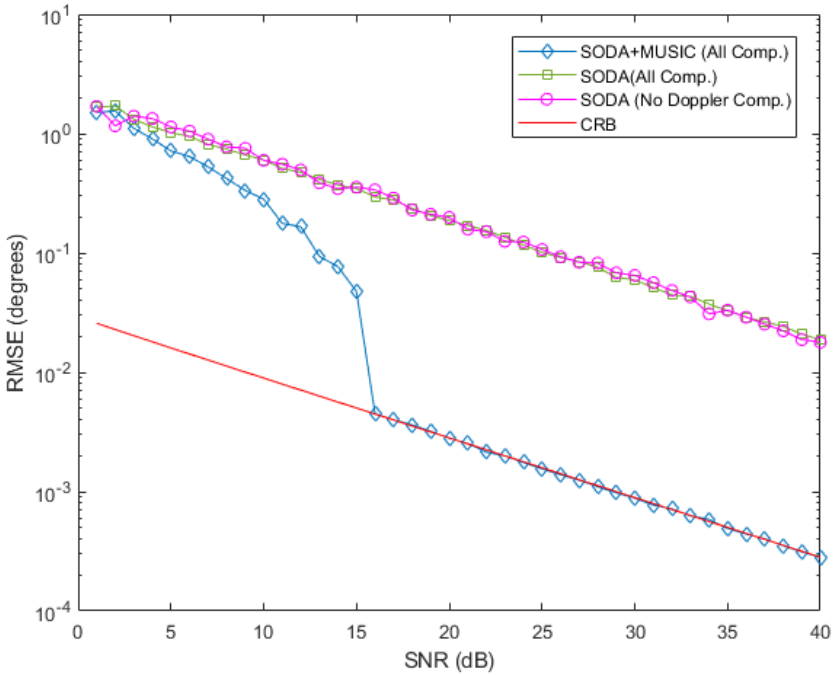

Figure 3.32. $M = 4$

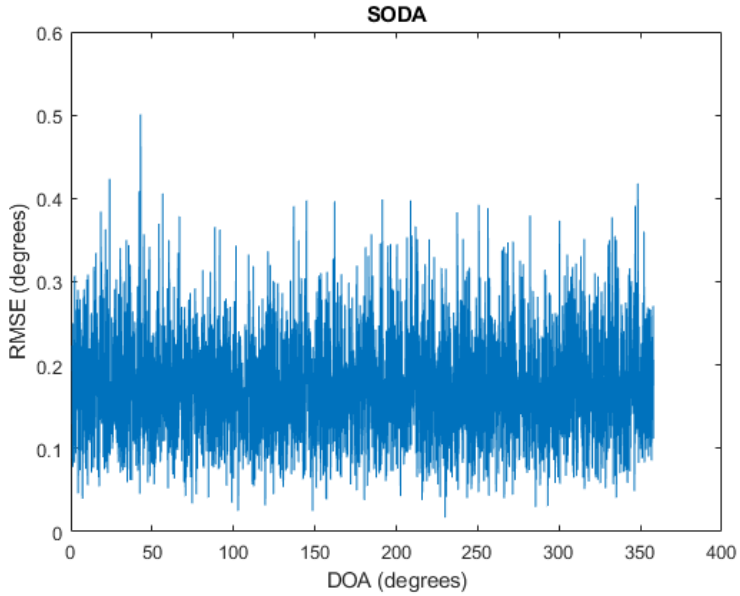

Figure 3.33. $M = 4, SNR = 20$ dB

CHAPTER 4

CONCLUSION

In this thesis, the focus is on improving ambiguity resolution for large aperture arrays to enhance accuracy in direction-of-arrival (DOA) estimation. A four-element planar SODA array is employed to address ambiguity issues associated with large aperture arrays. This array structure, however, has limitations due to its narrow configuration, similar to a linear array, which affects its performance at end-fire angles.

To overcome this limitation, we propose rotating the four-element array. This rotation introduces the Doppler Effect as a new parameter that must be corrected. We analyzed this approach using the Cramér-Rao Bound and practical simulation results. Our findings indicate that the performance of the SODA array can be significantly improved by incorporating rotation.

The study highlighted the effects of phase disturbances resulting from time delay and Doppler shifts in rotating SODA arrays. A compensation method was developed to address these issues, improving the accuracy and stability of DOA estimation across varying operating conditions.

By incorporating the MUSIC (Multiple Signal Classification) algorithm into the rotating SODA array, this work demonstrated a significant increase in DOA accuracy. The hybrid system effectively behaves like a larger, virtual array, providing improved performance in terms of DOA estimation. However, it was also noted that phase imbalance due to Doppler effects hindered the convergence of the system's performance to the Cramer-Rao Bound in certain cases.

The research showed that after Doppler compensation, the rotating MUSIC algorithm yielded close-to-optimum DOA estimation, with the estimation

error converging to the Cramer-Rao Bound. Although the rotating SODA array was less affected by Doppler shifts, the MUSIC algorithm showed considerable improvement after Doppler compensation. The simulation results confirmed that the SODA-MUSIC hybrid approach outperformed the pure time-delay compensated case, providing more accurate and robust DOA estimates, particularly in the presence of Doppler shifts. The study highlighted the effects of phase disturbances resulting from time delay and Doppler shifts in rotating SODA arrays. A compensation method was developed to address these issues, improving the accuracy and stability of DOA estimation across varying operating conditions.

This thesis has contributed to the understanding of rotating SODA arrays and the application of the MUSIC algorithm in improving DOA estimation performance. The proposed methods, including Doppler and time-delay compensation, significantly enhance the reliability and accuracy of DOA estimation in rotating systems.

This array structure and its rotation mechanism offer substantial benefits for radar and electronic support measures (ESM) applications, especially at high operating frequencies with very short wavelengths. Given the impracticality of constructing an antenna array with $\lambda/2$ spacing when wavelengths are very small, ambiguity issues arise. The proposed array structure combines the advantages of rotation and SODA, effectively resolving ambiguities over a 360° field of view (FOV), and achieving integration gains by creating a virtual array. It also provides an isotropic array response. Furthermore, the use of super-resolution algorithms enables performance close to the CRB. Future work could explore further optimizations in the compensation techniques and expand the integration of advanced signal processing algorithms to achieve even higher performance in real-world applications.

.

REFERENCES

[1] H. L. V. Trees, Optimum Array Processing, New York: John Wiley & Sons, Inc., 2002.

[2] D. Schleher, Electronic Warfare in the Information Age, Boston: Artech House, INC, 1999.

[3] J. Tsui, Digital Techniques for Wideband Receivers, Boston: SciTech Publishing Inc., 2004.

[4] P. Q. C. Ly, «Fast and Unambiguous Direction Finding for Digital Radar Intercept Receivers,» Adelaide, 2013.

[5] Y. h. Li, X. d. He and B. Tang, "A method for ambiguity solving based on rotary interferometer," in *International Conference on Communications, Circuits and Systems (ICCCAS)*, Chengdu, 2013.

[6] A. Orduyilmaz, M. Serin, A. C. Gürbüz and A. Yildirim, "Passive direction finding using amplitude and phase comparison techniques," in *22nd Signal Processing and Communications Applications Conference (SIU)*, Trabzon, 2014.

[7] A. V. İpek, «IMPLEMENTATION OF A DIRECTION FINDING ALGORITHM,» Ankara, 2006.

[8] A. E. Gürel, A. Orduyilmaz, M. Serin, A. Yildirim and G. Soysal, "Real time ambiguity resolution in hybrid amplitude/phase comparison direction finding systems," in *26th Signal Processing and Communications Applications Conference (SIU)*, Izmir, 2018.

[9] O. Tutaysalgır, A. Orduyılmaz, M. S. K. Öktem and A. Yıldırım, "Real time wideband direction finding," in *23nd Signal Processing and Communications Applications Conference (SIU)*, Malatya, 2015.

[10] A. E. Gürel, A. Orduyılmaz, S. A. Yıldırım, G. Kara, M. Serin, İ. E. Ortatatlı and A. Yıldırım, "Real time passive direction finding in FPGA environment," in *25th Signal Processing and Communications Applications Conference (SIU)*, Antalya, 2017.

[11] A. Orduyılmaz, M. Serin, A. Yıldırım, K. Ceyhan and A. C. Gürbüz, "Hybrid phase amplitude direction finding method," in *23nd Signal Processing and Communications Applications Conference (SIU)*, Malatya, 2015.

[12] A. Orduyilmaz, G. Kara, A. E. Gürel, M. Serin, A. Yildirim and G. Soysal, "Real time four channel phase comparison direction finding method," in *26th Signal Processing and Communications Applications Conference (SIU)*, Izmır, 2018.

[13] R. Schmidt, "Multiple emitter location and signal parameter estimation," *IEEE Transactions on Antennas and Propagation*, vol. 34, pp. 276-280, 1986.

[14] D. Li, Y. Jiao, Z. Gao, F. Mao and H. Zhang, "Study on Improving the Direction-Finding Accuracy of Rotary Baseline Phase Interferometer," in *IEEE 4th Advanced Information Management, Communicates, Electronic and Automation Control Conference (IMCEC)*, Chongqing, 2021.

[15] M. Lin, P. Liu and J. Liu, "DOA ambiguity suppressing by rotating the array," in *2015 IEEE 4th Asia-Pacific Conference on Antennas and Propagation (APCAP)*, Bali, 2015.

[16] P. Q. C. Ly, S. D. Elton, D. A. Gray and J. Li, "Unambiguous AOA estimation using SODA interferometry for electronic surveillance," in *2012*

IEEE 7th Sensor Array and Multichannel Signal Processing Workshop (SAM), Hoboken, NJ, 2012.

[17] M. N. E. I. Rouabhia, A. Bellabas, M. L. Bencheikh and M. E. M. Abdelaziz, "On the phase interferometry direction finding: Performance comparison and FPGA implementations," in *Seminar on Detection Systems Architectures and Technologies (DAT)*, Algiers, 2017.

[18] B. Güney, Ö. S. coşkun, A. E. Gürel and A. Orduyılmaz, "Improving Direction Finding Performance with SBI Algorithm in Interferometry Method," in *31st Signal Processing and Communications Applications Conference (SIU)*, Istanbul, 2023.

[19] J. Xin, G. Liao, Z. Yang and H. Shen, "Ambiguity Resolution for Passive 2-D Source Localization with a Uniform Circular Array," *Sensors*, vol. 18, no. 8, p. 2650, 2018.

[20] T. Kabzinski and E. A. P. Habets, "A Least Squares Narrowband DOA Estimator with Robustness Against Phase Wrapping," in *27th European Signal Processing Conference (EUSIPCO)*, A Coruna, 2019.

[21] P. Stoica, E. Larsson and A. Gershman, "The Stochastic CRB for Array Processing: A Textbook Derivation," *IEEE Signal Processing Letters*, vol. 8, no. 5, pp. 148-150, 2001.

[22] X. Lan, L. Wan, G. Han and J. J. P. C. Rodrigues, "A Novel DOA Estimation Algorithm Using Array Rotation Technique," *Future Internet*, vol. 6(1), pp. 155-170, 2014.

[23] N. A. Baig, M. B. Malik, M. Zeeshan, M. Z. U. Khan and M. A. Ajaz, "Efficient Target Detection and Joint Estimation of Target Parameters With a Two-Element Rotating Antenna," *IEEE Access*, vol. 4, pp. 4442-4451, 2016.

[24] İ. E. Ortatatlı, A. Orduyılmaz, M. Serin, Ö. Özdil, A. Yıldırım and A. C. Gürbüz, "Real-time frequency parameter extraction for electronic support systems," in *24th Signal Processing and Communication Application Conference (SIU)*, Zonguldak, 2016.